*Article*

# Comparison of the Power Extraction Performance of an Oscillating Hydrofoil Turbine with Different Deflector Designs

**Arun Raj Shanmugam** [1] ![ORCID], **Ki Sun Park** [1,2] ![ORCID] **and Chang Hyun Sohn** [3,*] ![ORCID]

1   Department of Mechanical and Aerospace Engineering, United Arab Emirates University,
    Al Ain 15551, Abu Dhabi, United Arab Emirates; arunraj.v2009@gmail.com (A.R.S.);
    kisunpark@uaeu.ac.ae (K.S.P.)
2   National Space Science and Technology Center (NSSTC), United Arab Emirates University,
    Al Ain 15551, Abu Dhabi, United Arab Emirates
3   School of Mechanical Engineering, Kyungpook National University, Daegu 41566, Republic of Korea
*   Correspondence: chsohn@knu.ac.kr

**Abstract:** The unsteady RANS equations for a two-dimensional hydrofoil were solved using ANSYS Fluent to model and simulate the hydrofoil at a constant Reynolds number, $Re$, of $2 \times 10^5$ and a fixed reduced frequency, $f^*$, of 0.14. The simulations were performed by varying parameters, such as the number of deflectors $N$, tilt angle of the deflectors $\beta$, and vertical spacing of the deflectors $J^* = J/c$, to determine the effect of the upstream deflector's position on the hydrofoil's performance. The results demonstrated that the deflector was effective at redirecting the separated flow away from the edges, which was then amplified downstream before colliding with the leading edge of the oscillating hydrofoil to increase power extraction. The performance of the oscillating hydrofoil was highly reliant on all three studied parameters. The hydrofoil with two deflectors ($N = 2$) displayed marginally superior power extraction capability compared to the hydrofoil with a single deflector ($N = 1$). Furthermore, the hydrofoil with the rightward inclined deflector at a low tilt angle ($-5° \geq \beta \geq -10°$) exhibited relatively better power extraction performance than the others. The best deflector design increased the hydrofoil's cycle-averaged power coefficient by approximately 32% compared to a hydrofoil without a deflector. The vortex structures revealed that the flow evolution and power extraction performance were dependent on the size, robustness, and growth rate of the leading edge vortex (LEV) as well as the timing of LEV separation. The power extraction efficiency of an oscillating hydrofoil increased in the mid downstroke and upstroke due to the formation of a more robust LEV when the hydrofoil–deflector interaction was advantageous, but it dropped in the wing reversal due to the early separation of the LEV when the hydrofoil–deflector interaction was counterproductive.

**Keywords:** deflector; flapping wing; FSI; oscillating wing; tidal turbine; renewable energy

## 1. Introduction

The 2015 Paris Climate Conference (COP21) set the path for a new international climate accord to prevent disastrous climate change by limiting global warming to less than 2 degrees Celsius. The agreement also sought to strengthen the nations' ability to counteract the effects of climate change and promote low-carbon, climate-resilient growth [1]. To attain these goals, research communities around the world are committed to developing low-cost renewable energy technologies. Hydrokinetic energy is very appealing due to its huge potential to deliver power reliably. The global hydrokinetic energy potential was estimated to be 1000 GW [2]. Commonly, rotary turbines are utilized at inlets, straits, headlands, and channels between islands to harvest this hydrokinetic energy [3]. Among other benefits, the high density of water can render these devices smaller.

The advantages offered by oscillating hydrofoils, especially in shallow-water applications, render them an intriguing and novel form of hydrokinetic energy technology. The

oscillating hydrofoil solves the issue of high tip speed at a large radius without significant centrifugal stress [4]. The hydrofoil's motion parameters are the primary determinants of the power extracted, suggesting that a complex foil shape is unnecessary. However, due to the complexity of the system, the design and optimization of a hydrofoil that could oscillate in flight can be practically challenging.

Xiao and Zhu [5] and Young et al. [6] have both provided in-depth reviews of the concept of oscillating wind turbines. Furthermore, Kinsey and Dumas [7] conducted a parametric study using the NACA 0015 airfoil at $Re = 1.1 \times 10^3$ to determine the optimum kinematic parameters of the oscillating wing. The authors mapped the power extraction efficiency $\eta$ over a large range of reduced frequency $0 < f^* < 0.25$ and pitch amplitude $0° < \theta_o < 90°$ and found that the highest value was at $f^* = 0.14$–$0.15$ and $\theta_o = 75°$. Zhu [8] examined the relationship between the wake stability and power extraction performance of an oscillating wing using a Joukowski airfoil at $Re = 10^3$. The growth of the vortex structures was intimately related to the efficiency of power extraction, and the maximum power extraction efficiency was observed when the oscillation frequency of the wing $f$ matched the wake frequency $f_w$. In fact, the results indicated that the oscillating wing did not require any activation, validating the viability of developing a fully passive system to obtain more efficiency. Wang et al. [9] conducted a numerical simulation to examine the influence of wing shape on the power extraction capability of an oscillating wing at $Re = 1.38 \times 10^4$. The authors evaluated a range of wing profiles from the NACA 4 and NACA 6 series and concluded that symmetrical wings may extract more power than asymmetric wings.

Using non-sinusoidal wing kinematics, a number of researchers [10–13] managed to enhance the power extraction performance of an oscillating wing. Xiao et al. [10] ran numerical simulations to examine the effect of the non-sinusoidal pitch profile on the power extraction performance of an oscillating wing harvester at $Re = 10^4$. It was found that the ideal pitch motion profile increased the power extraction efficiency by almost 50%. Lu et al. [11] studied the influence of non-sinusoidal motion on the power extraction performance of an oscillating wing with an NACA 0012 airfoil at $Re = 10^4$. Various non-sinusoidal motion profiles were examined, and results showed that the performance of the oscillating wing was superior when the toothed heaving profile and the square pitching profile were used. Using both experimental and numerical methods, Lu et al. [12] examined the flow development and power extraction performance of an oscillating wing with a trapezoidal pitch motion profile at $Re = 3.5 \times 10^3$. The flow field was visualized using the particle image velocimetry method. An increase in the heaving amplitude $H_o$ at a constant reduced frequency $f^*$ was found to increase the power coefficient and decrease power extraction efficiency. At a fixed pitch amplitude $\theta_o$, the efficiency was also found to increase as the reduced frequency $f^*$ was increased, up to a maximum, and then decrease. Veilleux and Dumas [13] investigated a hydrokinetic turbine that uses the pitch–heave oscillations of an elastically mounted, symmetrical, and rigid airfoil. Performing gradient-like optimization, two-dimensional efficiencies as high as 34% have been achieved, and two basic mechanisms—adequate synchronization between both degrees of freedom and the non-sinusoidal pitching motion—have been found to improve turbine performance.

Few studies [14,15] have modified the wing's oscillation trajectory to test its impact on power extraction efficiency. Ma et al. [14] proposed a modified wing motion of an arc trajectory for an oscillating hydrofoil. The NACA 0015 airfoil was used in the simulations, and the Reynolds number $Re$ was set to $5 \times 10^5$. Using the optimal design (arc radius $R = 1$ m, heave amplitude $H_o = 10°$, $f^* = 0.15$, and $\theta_o = 70°$), the oscillating wing could attain a maximum power extraction efficiency of 35.27%. Sitorus and Ko [15] recently compared the power extraction performance of an oscillating hydrofoil for three separate movements at $Re = 1.7 \times 10^6$: linear, left-swing, and right-swing. The left-swing motion was found to outperform both the linear and right-swing motions in terms of power extraction. Using numerical analysis, Kinsey and Dumas [16] investigated the power extraction performance of an oscillating tandem hydrofoil at $Re = 5 \times 10^5$. The "global phase shift" $\Psi$ parameter

was used to integrate the effects of two separate parameters, namely local phase shift $\psi$ and wing spacing $L^*$. The authors demonstrated that a tandem oscillating hydrofoil operating at the same flow window could achieve an efficiency of up to approximately 64%.

Recently, Picard-Deland et al. [17] prescribed large heaving amplitudes in conjunction with a modified pitching motion that imposes a sinusoidal evolution of the angle of attack to enhance the energy extraction of an oscillating foil. At large heave amplitude ($15c$), a single foil can achieve efficiency as high as 44%, equivalent to 10 foils flapping at small heave amplitude ($1c$). By altering the pitching function to maintain a high angle of attack for a longer period of the cycle, efficiency can reach 49%. Experimental research was conducted by Oshkai et al. [18] on a prototype of a self-sufficient flapping foil hydrokinetic turbine. The foil experienced pitch and heave oscillations in water at $Re = 2.1 \times 10^4$, with the oscillations elastically restricted. Below a threshold of reduced frequency of the incoming vortices, stable operation of the turbine was achieved. When the frequency of the disturbance in the upstream flow was greater than the threshold frequency, the turbine oscillated unsteadily.

Passive augmentation devices have also been employed to improve the flow and power extraction performance of the oscillating wing. Among them, several studies confirmed that the performance of the oscillating wing could be significantly improved when gurney flaps were added [19–23]. Previous research also investigated whether the passive geometries of the shroud [24] and duct [25,26] could improve the performance of the oscillating wing. Other studies also contributed to our understanding of the oscillating wing's aerodynamic characteristics and flow field [27–31]. However, it was evident that current research on passive augmentation devices to improve the performance of the oscillating wing was lacking. Consequently, the objective of the present study was to determine the optimal arrangement of an upstream flat plate deflector to enhance the performance of the oscillating wing.

A deflector was developed upstream of an oscillating hydrofoil turbine in order to improve the power extraction performance of the oscillating hydrofoil. Experiments and numerical simulations have been used in the past to test the effectiveness of upstream deflectors as augmentation devices in various turbines, including vertical axis wind turbines [32,33], Savonius water turbines [34,35], cross axis wind turbines [36], and drag-type hydrokinetic rotors [37]. Recent research conducted by Lahooti and Kim [38] examined the effect of the height of the upstream body $H^* = H/c$, horizontal spacing $I^* = I/c$, and vertical spacing $J^* = J/c$ of an upstream body on the power extraction performance of an oscillating wing windmill at $Re = 10^3$. The authors found that the maximum power coefficient could be obtained when $H$ and $I$ were equal to the chord length of the hydrofoil. The interaction between the vortices shed from the upstream body and the hydrofoil was the primary mechanism for improving efficiency.

The design of oscillating hydrofoil turbines relies heavily on precisely predicting vortex formations and power coefficients. The LBM-IBM has been well documented in the literature to simulate an oscillating hydrofoil turbine. However, this technique is often employed in low Reynolds number conditions [39–43]. Alternatively, BEM [44,45] was also used to solve the complex problem of fluid–structure interaction. This method is more affordable than others, but it suffers in terms of accuracy for specific operating parameter ranges [44,45]. One of the most well-known methods, RANS, predicts the behavior of an oscillating hydrofoil turbine with reasonable accuracy [7,14]. Only a small difference was observed in the average power coefficient between the RANS and SAS [46]. Although methods such as LES/DES are better than RANS in terms of model construction, they are computationally unaffordable for detailed parametric studies [47–49]. Against this backdrop, the RANS method was selected here to simulate the effect of an upstream deflector on an oscillating hydrofoil turbine.

In the present study, three independent parameters, namely the number of deflectors $N$, the tilt angle of the deflector $\beta$, and the vertical spacing of deflector $J^* = J/c$, were varied to configure a total of 61 cases for further investigation. These parameters were

indeed found to affect the performance of the oscillating hydrofoil. In addition, the ideal deflector design characteristics for the turbine were determined, and the flow fields were examined to determine the mechanism for enhancing the performance of power extraction. The Reynolds number *Re* of the flow was calculated to be $2 \times 10^5$ based on the chord length *c*. The acquired results could help us determine the applicability and effectiveness of upstream deflectors to enhance the power extraction performance of oscillating hydrofoils.

## 2. Numerical Methodology

An oscillating hydrofoil turbine operates on the fundamental principle of hydrodynamic force generation and pitch moment to extract energy from the incoming flow. Throughout the downstroke, the hydrofoil maintains a negative pitch angle to generate a negative lift, pushing it downwards. At the end of the downstroke (supination), the hydrofoil reverses its direction and begins the upstroke. Throughout the upstroke, the hydrofoil maintains a positive pitch angle to produce a positive lift, pushing it upwards. Consequently, the hydrodynamic force generated by the hydrofoil is always aligned to the direction of the hydrofoil motion. The flow does mechanical work on the hydrofoil, which can then be converted into electric power [7].

Oscillating hydrofoil turbines can benefit from the addition of devices that increase the flow and power extraction. A deflector plate upstream of the hydrofoil could be regarded as a straightforward and affordable option. Von Kármán vortices of clockwise and counterclockwise rotation were formed from the edges of the deflector when it was placed normal to the free-stream flow, and a wake was also formed behind the deflector. It was found that although there was a region of low pressure and velocity within the wake, the velocity was much higher in the region immediately outside the near wake [38].

As indicated in Figure 1, a deflector was positioned upstream of the oscillating hydrofoil to augment its power extraction performance. The geometric parameters affecting the performance include the height of the upstream deflector *H\**, the horizontal spacing between the deflector and hydrofoil *I\**, the vertical spacing between the deflector and hydrofoil *J\**, and the tilt angle of the deflector *β*. The number of deflectors, *N*, may also play a role in the enhancement mechanism beyond the aforementioned variables. The upstream deflectors can be installed in an inclined position in the leftward or rightward direction (from the reference axis). A positive tilt angle would mean that the deflector was inclined to the left, and a negative tilt angle would mean that the deflector was inclined to the right. As in prior research, we used the NACA 0015 airfoil shape for the oscillating hydrofoil [7,14].
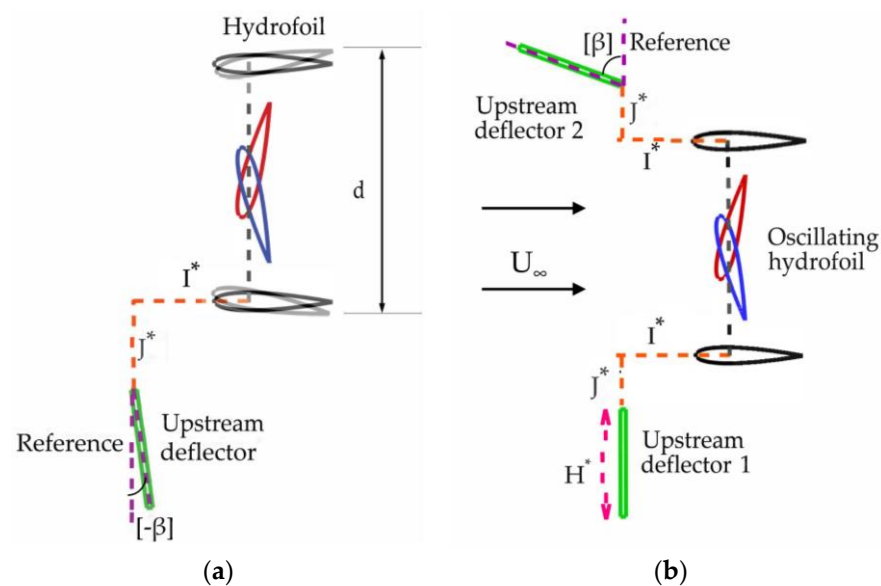


**Figure 1.** Schematic of the oscillating hydrofoil with an upstream deflector (the red and blue foils represent downstroke and upstroke motion, respectively). (**a**) Single design, (**b**) dual design.

Various designs of deflectors such as flat plate [32,34–38], semi-circular [50], curved [51], and rhombus [33] were considered in past studies to improve the performance. In this study, a single/dual flat plate deflector of height $1c$ and thickness $0.05c$ at various inclinations was employed. Using a flat plate deflector design will offer great flexibility for the designer in determining the vortex interaction between the hydrofoil and deflector, a key factor influencing the oscillating hydrofoil's performance positively. Moreover, this type of deflector has other advantages in terms of design, stiffness, less material, and low production cost [32–38].

The motion of the oscillating hydrofoil can be described by the simultaneous heave motion $H(t)$ and pitch motion $\theta(t)$, as illustrated in Figure 1, which can be written mathematically using Equations (1) and (2), as follows:

$$H(t) = H_o \sin(\omega t + \varphi) \tag{1}$$

$$\theta(t) = \theta_o \sin(\omega t) \tag{2}$$

Here, $H(t)$ denotes the instantaneous heave amplitude, $\theta(t)$ is the instantaneous pitch amplitude, $H_o/c$ is the maximum heave amplitude (=1), $\theta_o$ is the maximum pitch amplitude (=76°), $\varphi$ represents the phase difference between heaving and pitching motions ($\varphi$ = 90°), and $\omega$ is the oscillation frequency ($2\pi ft$). The pitch axis of the oscillating hydrofoil was situated at $1/3$ of the chord length $c$ from its leading edge LE.

The frequency of the oscillating hydrofoil can be characterized by using the reduced frequency $f^*$, as shown in Equation (3). The Reynolds number $Re$ of the flow can be computed from Equation (4), and the surface pressure around the hydrofoil can be characterized by the pressure coefficient $C_{P(x/c)}$, as shown in Equation (5).

$$f^* = \frac{fc}{U_\infty} \tag{3}$$

$$Re = \frac{\rho U_\infty c}{\mu} \tag{4}$$

$$C_{P(x/c)} = \frac{P(x/c) - P_\infty}{0.5\rho U_\infty^2} \tag{5}$$

Here, $c$ represents the chord length, $U_\infty$ is the free-stream velocity of the fluid, $\rho$ is the fluid density, $\mu$ is the dynamic viscosity of the fluid, $P_{(x/c)}$ is the static pressure along the surface of the oscillating hydrofoil, and $P_\infty$ is the free-stream static pressure.

The effective angle of attack $\alpha_E$ and the nominal angle of attack $\alpha_N$ can be expressed as follows:

$$\alpha_E(t) = \theta(t) - \tan^{-1}\left(\frac{V_Y(t)}{U_\infty}\right) \tag{6}$$

$$\alpha_N = \left| \theta_o - \tan^{-1}\left(\frac{\omega V_Y}{U_\infty}\right) \right| \tag{7}$$

where $V_Y$ represents the heaving velocity of the hydrofoil.

The total power extracted from the flow comprises two components: pitch motion and heave motion, as given by Equation (8).

$$P(t) = [F_Y(t)V_Y(t) + M(t)\dot{\theta}(t)] \tag{8}$$

where $P(t)$ represents the instantaneous power extracted from the flow, $F_Y(t)$ is the instantaneous lift force, $M$ is the instantaneous pitch moment and $\cdot$ is a first-order derivative.

The lift coefficient $C_L$, drag coefficient $C_D$, moment coefficient $C_M$, and power coefficient $C_P$ can be computed from Equations (9)–(12).

$$C_L(t) = \frac{F_Y(t)}{\frac{1}{2}\rho U_\infty^2 c} \tag{9}$$

$$C_D(t) = \frac{F_X(t)}{\frac{1}{2}\rho U_\infty^2 c} \tag{10}$$

$$C_M(t) = \frac{M(t)}{\frac{1}{2}\rho U_\infty^2 c^2} \tag{11}$$

$$C_P(t) = \frac{P(t)}{P_{ref}} \tag{12}$$

Here, $F_X(t)$ denotes the instantaneous drag force and $C_P$ the power coefficient.

Conventionally, the maximum power available for generation in oscillating hydrofoils is given by $0.5\rho dU_\infty^3$. Here, $d$ is the overall distance swept by the hydrofoil ($d = 2.55c$), as shown in Figure 1a. However, oscillating hydrofoils with augmentation devices have recently gained interest [38]. The primary purpose of augmentation devices such as upstream deflectors is to augment the flow, which will, in turn, help to increase the power extraction [32–38]. Therefore, using the traditional power coefficient definition is unsuitable for an oscillating hydrofoil with an upstream deflector, as the computed efficiencies would exceed the theoretical Betz limit of 59% [52,53]. A new definition of $P_{ref}$ was required for such turbines, as recently proposed by Li [53]. For this purpose, a duct was considered to enclose the turbine as well as other structures including deflector. The presence of a duct wall could improve the hydrofoil's performance due to the ground effect. However, a recent study found that the role of the ground effect may be minimal for oscillating hydrofoils [54]. Further, the flow augmentation in the duct considered here was minor due to smaller parabolic profile parameter $a$, and hence, the duct geometry was not included in the numerical procedure.

The reference power [53] can be expressed as follows:

$$P_{ref} = \rho\pi\frac{(aL^2+r)^6 U_\infty^3}{8L}\left(\frac{5\arctan\left(L\sqrt{\frac{a}{r}}\right)}{8r^{3.5}\sqrt{a}} + \frac{5L}{8r^3(r+aL^2)} + \frac{5L}{12r^2(r+aL^2)^2} + \frac{L}{3r(r+aL^2)^3}\right) \tag{13}$$

Here, $a$ denotes the duct profile parameter ($=0.01c$); $r$ the half overall vertical distance ($=3.275c$); $L$ the half-length of duct ($=5c$). Other details of the duct wall can be found in Li [53].

The ratio of efficiencies between the oscillating hydrofoil with the upstream deflector to the baseline oscillating hydrofoil can be computed from Equation (14).

$$\frac{\eta}{\eta_b} = \frac{\overline{C_P}}{C_{P,b}} \tag{14}$$

The commercial code ANSYS Fluent was used to solve the Reynolds-averaged Navier–Stokes (RANS) flow equations for an oscillating hydrofoil with a deflector placed in the upstream direction. The RANS equations for unsteady and incompressible flow are described by Equations (15) and (16). The $k$-$\omega$ SST turbulence model was used to solve the Reynolds stress tensor in Equation (16) because it could accurately predict the timing and amount of flow separation, making it more suitable to perform the numerical simulations in the present study. This model uses a blending function to switch from the standard $k$-$\omega$ model near the wall to a high-Reynolds number $k$-$\varepsilon$ model in the outer region of the boundary layer [55].

$$\frac{\partial\rho}{\partial t} + \frac{\partial(\rho u_i)}{\partial x_i} = 0 \tag{15}$$

$$\frac{\partial}{\partial t}(\rho u_i) + \frac{\partial}{\partial x_j}(\rho u_i u_j) = -\frac{\partial p}{\partial x_i} + \frac{\partial}{\partial x_j}\left(\mu\left(\frac{\partial u_i}{\partial x_j} + \frac{\partial u_j}{\partial x_i} - \frac{2}{3}\delta_{ij}\frac{\partial u_l}{\partial x_l}\right)\right) + \frac{\partial}{\partial x_j}(-\rho\overline{u_i' u_j'}) \quad (16)$$

The flow field was solved using the finite volume method with a pressure-based solver. The Pressure-Implicit with Splitting of Operators (PISO) scheme was employed for the pressure–velocity coupling. A second-order scheme was used for the spatial discretization of pressure. A second-order upwind scheme was used for the spatial discretization of momentum and turbulence kinetic energy $k$ and specific dissipation rate $\omega$. An implicit first-order scheme was used for the discretization of unsteady terms.

A rectangular computational domain was adopted in the simulation with length $l$ ($-15\,c \leq l \leq 45\,c$) and breadth $b$ ($-30\,c \leq b \leq 30\,c$), as shown in Figure 2. The domain was divided into two zones: the hydrofoil zone and a buffer zone with a non-conformal sliding interface. The hydrofoil zone underwent a rigid body motion, while the buffer zone was re-meshed when the mesh deformation occurred. The hydrofoil zone and the interface edge (interface side 1), corresponding to the hydrofoil zone, underwent both heave and pitch motion. Meanwhile, the shadow interface edge (interface side 2) corresponding to the buffer zone underwent pure heave motion. By adopting this strategy, one can avoid the mesh deformation in the buffer zone caused by the pitch motion of the oscillating hydrofoil. Spring-based smoothing and remeshing techniques of the dynamic mesh method were used to update the mesh deformed by the heave motion of the shadow interface. A spring constant of 0.01 was used in the smoothing method. This ensured that the cells far away from the moving zone deform more than the nearby cells, thereby retaining mesh quality near the moving zone. Many variables, such as minimum and maximum length scales and maximum cell skewness zone, decide the local remeshing of the cells. The minimum length scale was selected from the value of minimum cell edge length, while the maximum scale length was maintained at 10 times the minimum length scale. The maximum skewness of the deformed mesh during remeshing was restricted to 0.6. The simulations were run with the left boundary set to the velocity inlet, the right boundary set to the pressure outlet, and the side boundaries set to symmetry. The hydrofoil and upstream deflector were subjected to a no-slip wall boundary condition. The boundary layer effects were modeled using structured quadrilateral mesh cells of O-type around the hydrofoil, while the remaining regions of the domain were modeled using the unstructured triangular mesh cells. The first cell layer was placed at $1.05 \times 10^{-4}\,c$ from the hydrofoil's surface, yielding a $Y^+$ of approximately 1. Assigning the O-grid a growth rate of 1.08 helped guarantee that a sufficient number of cells were contained within the boundary layer.

To evaluate the mesh dependence of the numerical results, three types of mesh were constructed: $M_1$ medium, $M_2$ fine, and $M_3$ refined, and their time-averaged results are compared in Table 1. The simulations were performed using the following hydrofoil motion parameters: $H_o/c = 1$, $\theta_o = 76°$, $\varphi = 90°$, $f^* = 0.14$, and $Re = 2 \times 10^5$. It can be noticed from Table 1 that there was a substantial change in the recorded data ($\overline{C_D}$, $\hat{C}_L$, and $\overline{C_P}$) between the $M_1$ and $M_2$ types of mesh. However, as the number of mesh cells was further increased ($M_2$–$M_3$), only a minor change was noticed in the recorded data. Hence, the fine mesh $M_2$ was sufficient to perform further simulations on spatial accuracy. Additionally, three time-step sizes ($T/500$, $T/1000$, and $T/2000$) were tested for the $M_2$ mesh, and their results are also compared in Table 1. The maximum error observed in the data recorded between $T/1000$ and $T/2000$ was approximately 1.4%. Hence, a time-step size of $T/1000$ was selected as the time-step size for further simulations.
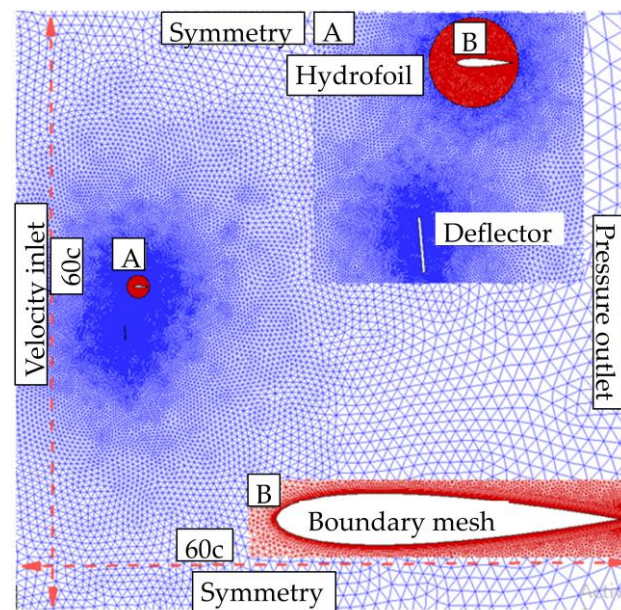
**Figure 2.** Computational domain, mesh distribution, and boundary conditions for a two-dimensional oscillating hydrofoil turbine with a single upstream deflector. Total cell count: 95,000 (360 on the hydrofoil).

**Table 1.** Comparison of time average force and power coefficients for different mesh sizes and time-step sizes (number of cells ($N_{cell}$) was rounded-off).

| Case | $N_{cell} \times 10^{-3}$ | $\Delta t$ | $\overline{C_P}$ | $\overline{C_D}$ | $\hat{C}_L$ |
|---|---|---|---|---|---|
| $M_1$: medium | 45 | $T/1000$ | 0.791549 | 2.118 | 2.674 |
| $M_2$: fine | 90 | $T/500$ | 0.762676 | 2.027 | 2.582 |
| | 90 | $T/1000$ | 0.808451 | 2.163 | 2.728 |
| | 90 | $T/2000$ | 0.816901 | 2.194 | 2.765 |
| $M_3$: refined | 135 | $T/1000$ | 0.811268 | 2.165 | 2.730 |

Four validation studies were performed to compare the present results with the reference, as shown in Figure 3, and confirm the accuracy of the numerical and mesh model used in the simulations. To begin, simulations of an oscillating hydrofoil on an arc trajectory for NACA 0015 were performed. The simulation settings were as follows: $H_o = 30°$, $\theta_o = 50°$, $f^* = 0.02$, $X_P/c = 1/3$, and $Re = 5 \times 10^5$, and the radius of the simulated arc was $R = 3$ m. The values of the force coefficients shown in Figure 3a, namely lift and drag, agreed with those calculated by Ma et al. [14].

Secondly, for NACA 0015, simulations were run with the oscillating hydrofoil following a linear trajectory. The simulation parameters were as follows: $H_o/c = 1$, $\theta_o = 60°$, $f^* = 0.18$, $X_P/c = 1/3$, and $Re = 1.1 \times 10^3$. The lift and power coefficients shown in Figure 3b were identical to those calculated by Kinsey and Dumas [7]. Next, simulations for NACA 0012 were performed with the oscillating hydrofoil pitching to compare the flow field. The following parameters were used for the simulation: $U_\infty = 1$ m/s, $\alpha_m = 24°$, $f = 0.25$ Hz, $k = 0.16$, and $Re = 2.4 \times 10^5$. The lift response in Figure 3c obtained from the present study had a good match with the results in Zheng et al. [56]. Further, the vorticity between the two studies also shows similar flow features. Finally, the simulations for NACA 0012 were performed with the oscillating hydrofoil heaving and pitching to compare with the experimental results of Simpson et al. [57]. The following parameters were used for the simulation: $U_\infty = 2.016$ m/s, $H_o/c = 1.23$, $\theta_o = 85.82°$, $f^* = 0.16$, and $Re = 1.38 \times 10^4$. As shown in Figure 3d, the lift response from the present simulations was close to the experi-

mental result of Simpson et al. [57] and the numerical study of Xu et al. [25]. So, the grid and the numerical model for the calculations were proven reliable and valid.
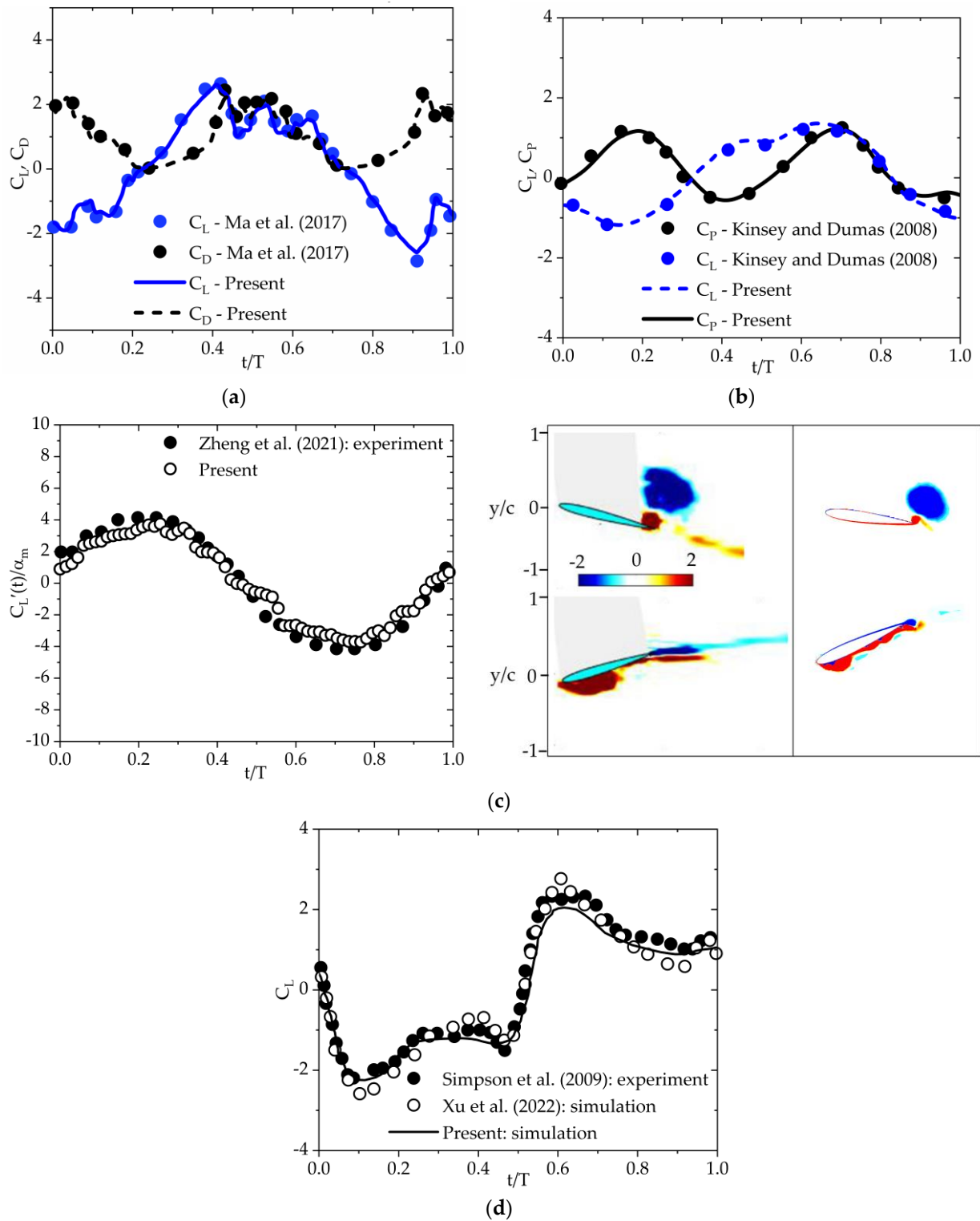


(**a**)



(**b**)



(**c**)



(**d**)

**Figure 3.** A comparison of force and power coefficients obtained from the present study with the findings of previous studies. (**a**) Present study vs. Ma et al. [14], (**b**) Present study vs. Kinsey and Dumas [7], (**c**) Present study vs. Zheng et al. [56], and (**d**) Present study vs. Simpson et al. [57] and Xu et al. [49].

## 3. Results and Discussion

A numerical investigation was carried out to estimate the optimal position of an upstream deflector in order to yield the maximum power extraction performance of an oscillating hydrofoil at $Re = 2 \times 10^5$. The hydrofoil's performance depends on several factors, including the number of deflectors $N$, the tilt angle of the deflector $\beta$, and the vertical spacing between the deflector and the hydrofoil $J^*$.

The geometry and schematic of the oscillating hydrofoil equipped with an upstream deflector are shown in Figure 1. The motion of the oscillating hydrofoil was modeled with sinusoidal functions, using the following parameters: $H_o/c = 1$, $\theta_o = 76°$, $\varphi = 90°$, and $f^* = 0.14$. Table 2 displays the results of our simulations with 61 different upstream deflector positions. It was decided that the deflector height $H^*$ and the horizontal spacing between the deflector and the hydrofoil $I^*$ would both be equal to 1. Subscripts 1 and 2 in Table 2 indicate the bottom deflector and top deflector, respectively.

**Table 2.** Parameters of the upstream deflector at various positions.

| # | $N$ | $H^*$ | $I_1^*$ | $I_2^*$ | $J_1^*$ | $J_2^*$ | $\beta_1°$ | $\beta_2°$ | # | $N$ | $H^*$ | $I_1^*$ | $I_2^*$ | $J_1^*$ | $J_2^*$ | $\beta_1°$ | $\beta_2°$ |
|---|---|---|---|---|---|---|---|---|---|---|---|---|---|---|---|---|---|
| 1 | 1 | 1 | 1 | | | | 0 | | 32 | 2 | 1 | 1 | 1 | | | 0 | 50 |
| 2 | 1 | 1 | 1 | | | | −2 | | 33 | 2 | 1 | 1 | 1 | | | 0 | 60 |
| 3 | 1 | 1 | 1 | | | | −5 | | 34 | 2 | 1 | 1 | 1 | | | 0 | 70 |
| 4 | 1 | 1 | 1 | | | | −10 | | 35 | 2 | 1 | 1 | 1 | 1/2 | 1 | 0 | 0 |
| 5 | 1 | 1 | 1 | | 1/4 | | −20 | | 36 | 1 | 1 | 1 | | | | 0 | |
| 6 | 1 | 1 | 1 | | | | 2 | | 37 | 1 | 1 | 1 | | | | −1 | |
| 7 | 1 | 1 | 1 | | | | 5 | | 38 | 1 | 1 | 1 | | | | −2 | |
| 8 | 1 | 1 | 1 | | | | 10 | | 39 | 1 | 1 | 1 | | | | −3 | |
| 9 | 1 | 1 | 1 | | | | 20 | | 40 | 1 | 1 | 1 | | | | −4 | |
| 10 | 2 | 1 | 1 | 1 | | | 0 | 0 | 41 | 1 | 1 | 1 | | | | −5 | |
| 11 | 2 | 1 | 1 | 1 | | | 0 | 10 | 42 | 1 | 1 | 1 | | | | −7.5 | |
| 12 | 2 | 1 | 1 | 1 | | | 0 | 20 | 43 | 1 | 1 | 1 | | | | −10 | |
| 13 | 2 | 1 | 1 | 1 | 1/4 | 1/4 | 0 | 30 | 44 | 1 | 1 | 1 | | 3/4 | | −15 | |
| 14 | 2 | 1 | 1 | 1 | | | 0 | 40 | 45 | 1 | 1 | 1 | | | | −20 | |
| 15 | 2 | 1 | 1 | 1 | | | 0 | 50 | 46 | 1 | 1 | 1 | | | | −30 | |
| 16 | 2 | 1 | 1 | 1 | | | 0 | 60 | 47 | 1 | 1 | 1 | | | | −40 | |
| 17 | 2 | 1 | 1 | 1 | | | 0 | 70 | 48 | 1 | 1 | 1 | | | | −50 | |
| 18 | 1 | 1 | 1 | | | | 0 | | 49 | 1 | 1 | 1 | | | | −60 | |
| 19 | 1 | 1 | 1 | | | | −2 | | 50 | 1 | 1 | 1 | | | | 2 | |
| 20 | 1 | 1 | 1 | | | | −5 | | 51 | 1 | 1 | 1 | | | | 5 | |
| 21 | 1 | 1 | 1 | | | | −10 | | 52 | 1 | 1 | 1 | | | | 10 | |
| 22 | 1 | 1 | 1 | | 1/2 | | −20 | | 53 | 1 | 1 | 1 | | | | 0 | |
| 23 | 1 | 1 | 1 | | | | 2 | | 54 | 1 | 1 | 1 | | | | −2 | |
| 24 | 1 | 1 | 1 | | | | 5 | | 55 | 1 | 1 | 1 | | | | −7.5 | |
| 25 | 1 | 1 | 1 | | | | 10 | | 56 | 1 | 1 | 1 | | | | −10 | |
| 26 | 1 | 1 | 1 | | | | 20 | | 57 | 1 | 1 | 1 | | 1 | | −20 | |
| 27 | 2 | 1 | 1 | 1 | | | 0 | 0 | 58 | 1 | 1 | 1 | | | | −30 | |
| 28 | 2 | 1 | 1 | 1 | | | 0 | 10 | 59 | 1 | 1 | 1 | | | | −40 | |
| 29 | 2 | 1 | 1 | 1 | 1/2 | 1/2 | 0 | 20 | 60 | 1 | 1 | 1 | | | | −50 | |
| 30 | 2 | 1 | 1 | 1 | | | 0 | 30 | 61 | 1 | 1 | 1 | | | | −60 | |
| 31 | 2 | 1 | 1 | 1 | | | 0 | 40 | | | | | | | | | |

### 3.1. Comparison of Hydrofoil's Power Extraction Efficiency at Various Deflector Positions

Figure 4 illustrates a comparison between the coefficients of lift, moment, and power of an oscillating hydrofoil with a deflector plate with the baseline values (no deflector plate). As shown, cases 1–17, cases 18–35, cases 36–52, and cases 53–61 correspond to the vertical spacing $J^*$ of 1/4, 1/2, 3/4, and 1, respectively. This investigation revealed that the power extraction performance of the oscillating hydrofoil depended heavily on all three upstream deflector parameters ($N$, $J^*$, and $\beta$). Depending on the deflector's position, it can be either constructive or destructive toward the hydrofoil's performance. The deflector's destructive effect in case 24 resulted in a mild degradation in power extraction performance, with the efficiency dropping by approximately 2.4%, as shown in Figure 4b. In contrast, case 42 exhibited the largest improvement in power extraction performance due to the deflector's constructive effect, with the efficiency increasing by 32% (refer to Figure 4c). Several other cases (3, 4, 15, 16, 37, 39–43, and 53) in Figure 4 also revealed a substantial improvement in the power extraction performance. Consequently, it could be inferred that the presence of properly positioned deflectors improved the power extraction performance of the oscillating hydrofoil. The power extraction capability of the dual upstream deflector hydrofoil was generally better than that of the single upstream deflector hydrofoil. Further, from Figure 4a–d, it can be noticed that by increasing the vertical spacing $J^*$ from 1/4 to 1/2, the power extraction efficiency dropped to a minimum and then rose to a maximum as $J^*$ increased to 3/4, then dropped again. In terms of power extraction, oscillating hydrofoils with deflectors tilted to the right between $-5°$ and $-10°$ performed better than those with deflectors tilted to the left. Further analysis of the instantaneous characteristics and flow field can shed light on the constructive or destructive effect of the deflector on the hydrofoil's performance.
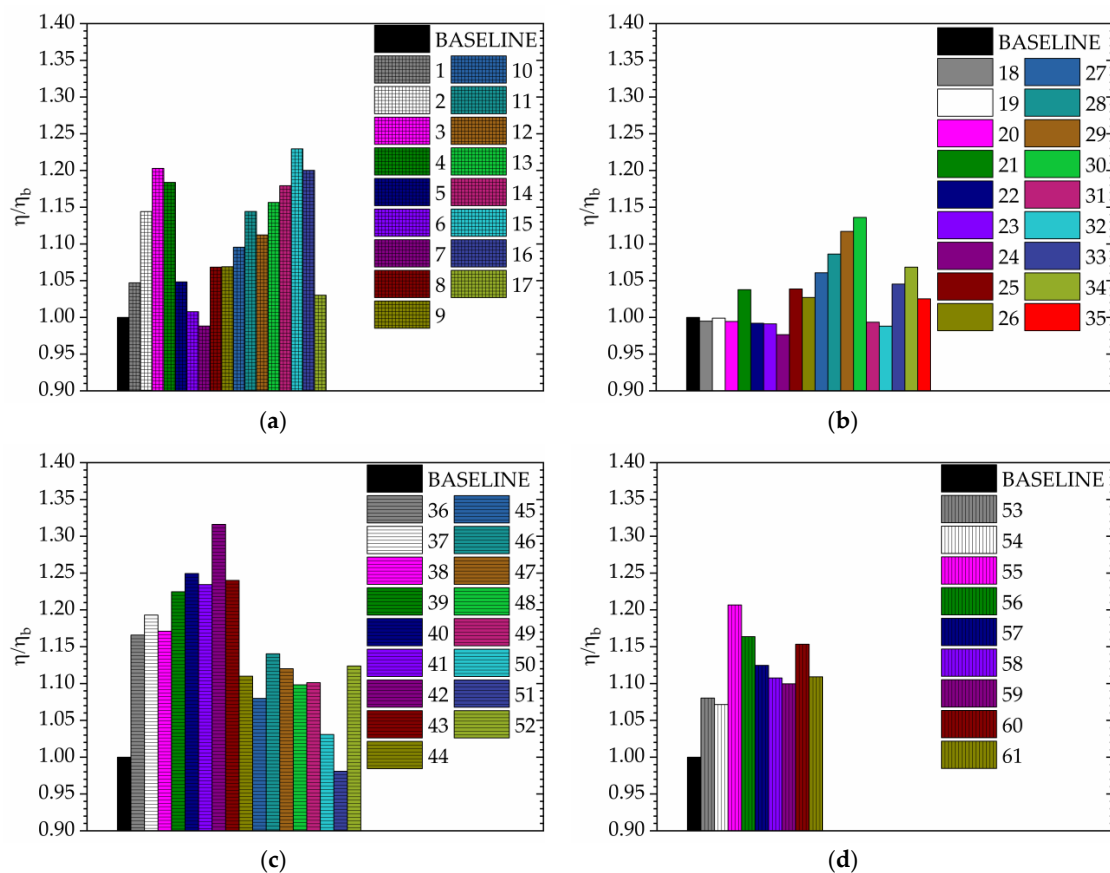


**Figure 4.** A comparison of the hydrofoil's power extraction performance at various deflector positions. (**a**) $J^* = 1/4$ shown by square pattern. (**b**) $J^* = 1/2$ shown by no pattern. (**c**) $J^* = 3/4$ shown by horizontal pattern. (**d**) $J^* = 1$ shown by vertical pattern.

*3.2. Performance Comparison of an Upstream-Deflector Hydrofoil with a Conventional Hydrofoil*

Figure 5 shows the comparison between the upstream-deflector hydrofoil and the conventional hydrofoil in terms of the time history of $C_L$, $C_{PY}$, $C_{P\theta}$, and $C_P$. The details of case 42 are as follows: $N = 1$, $I_1^* = 1$, $J_1^* = 3/4$, and $\beta = -7.5°$. Compared to the baseline hydrofoil, the upstream deflector-equipped hydrofoil displayed a relative efficiency improvement of approximately 32%. Figure 5 also demonstrates that the values of pitch power $C_P$ were slightly more negative than the ones for the conventional (baseline) hydrofoil, suggesting that the increase in lift forces and heave power $C_{PY}$ is due to the heave motion of the hydrofoil with an upstream deflector. The evolution of $C_{PY}$ and $C_P$ over time indicates that the upstream deflectors had the greatest impact on the hydrofoil efficiency in the middle of the stroke. The presence of upstream deflectors was found to increase the hydrofoil's lift forces at these specific times because they coincided with the hydrofoil's peak angle of attack.
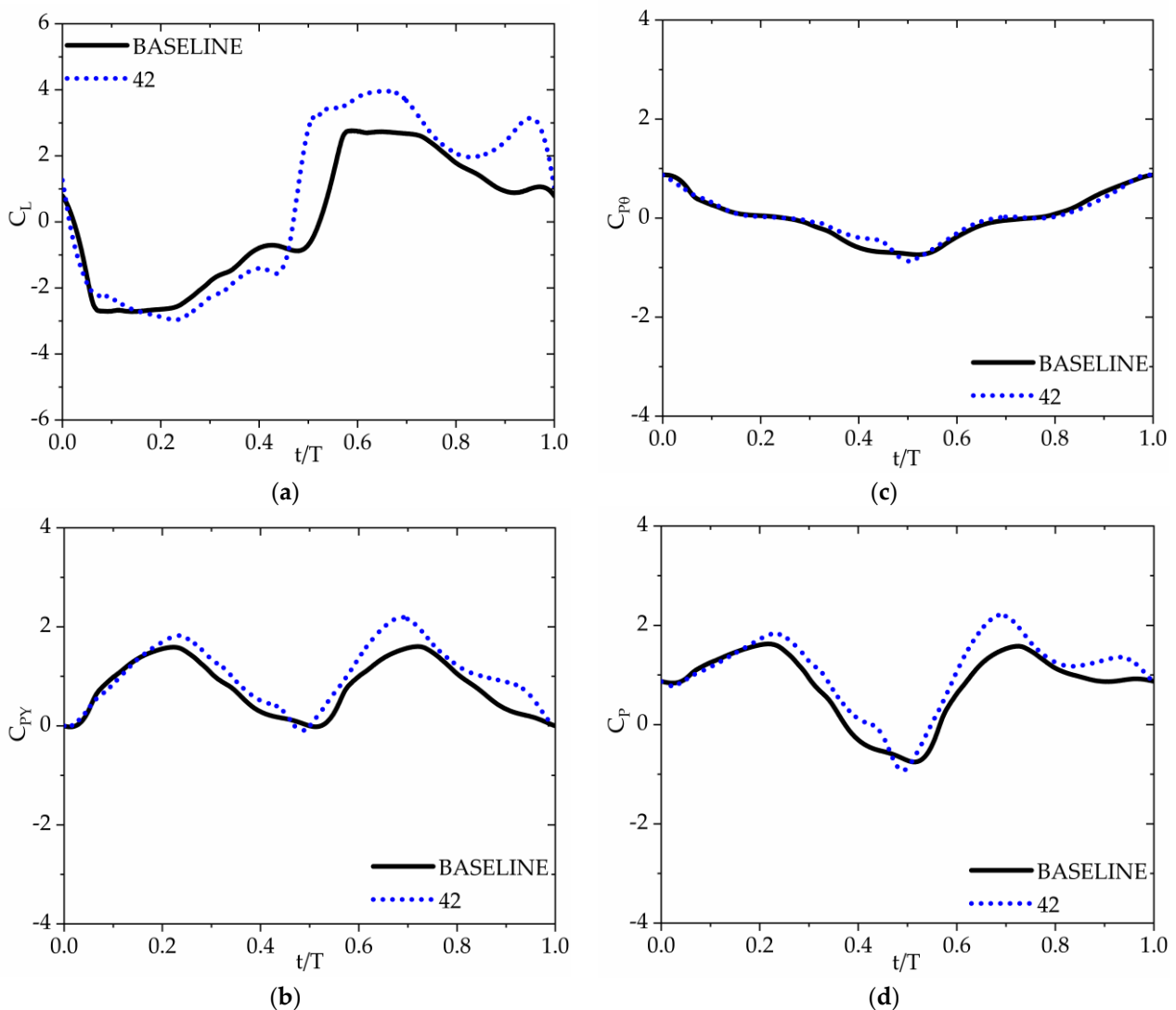


**Figure 5.** A comparison of the instantaneous lift and power coefficients between the upstream-deflector hydrofoil and the conventional hydrofoil (baseline). (**a**) Lift coefficient. (**b**) Heave power coefficient. (**c**) Pitch power coefficient. (**d**) Net power coefficient.

The variation in the instantaneous lift force and power coefficient for different deflectors can be understood by the vortex structures in Figure 6 and the static pressure plot in Figure 7. An oscillating wing can function in one of two modes, namely propulsion or

power extraction. The distinction between the two results from the direction of the forces created by the flow on the oscillating wing and can be derived from the feathering parameter $\chi$ $\left( \chi = \frac{\theta_o}{\arctan(2\pi f H_o / U_\infty)} \right)$. When an oscillating wing operates in the power-extraction regime ($\chi > 1$), it always generates drag (where average $C_X$ is positive). Under such conditions, the wake observed behind the wing looks like a von Kármán vortex street, which produces drag. Contrarily, when an oscillating wing operates in the propulsion regime ($\chi < 1$), it always generates thrust (where average $C_X$ is negative). The wake behind the wing looks like a reverse von Kármán vortex street, which produces thrust. In the present study, all of the cases simulated belonged to $\chi > 1$ and hence, only the drag-generating von Kármán-like vortex streets were observed [7].
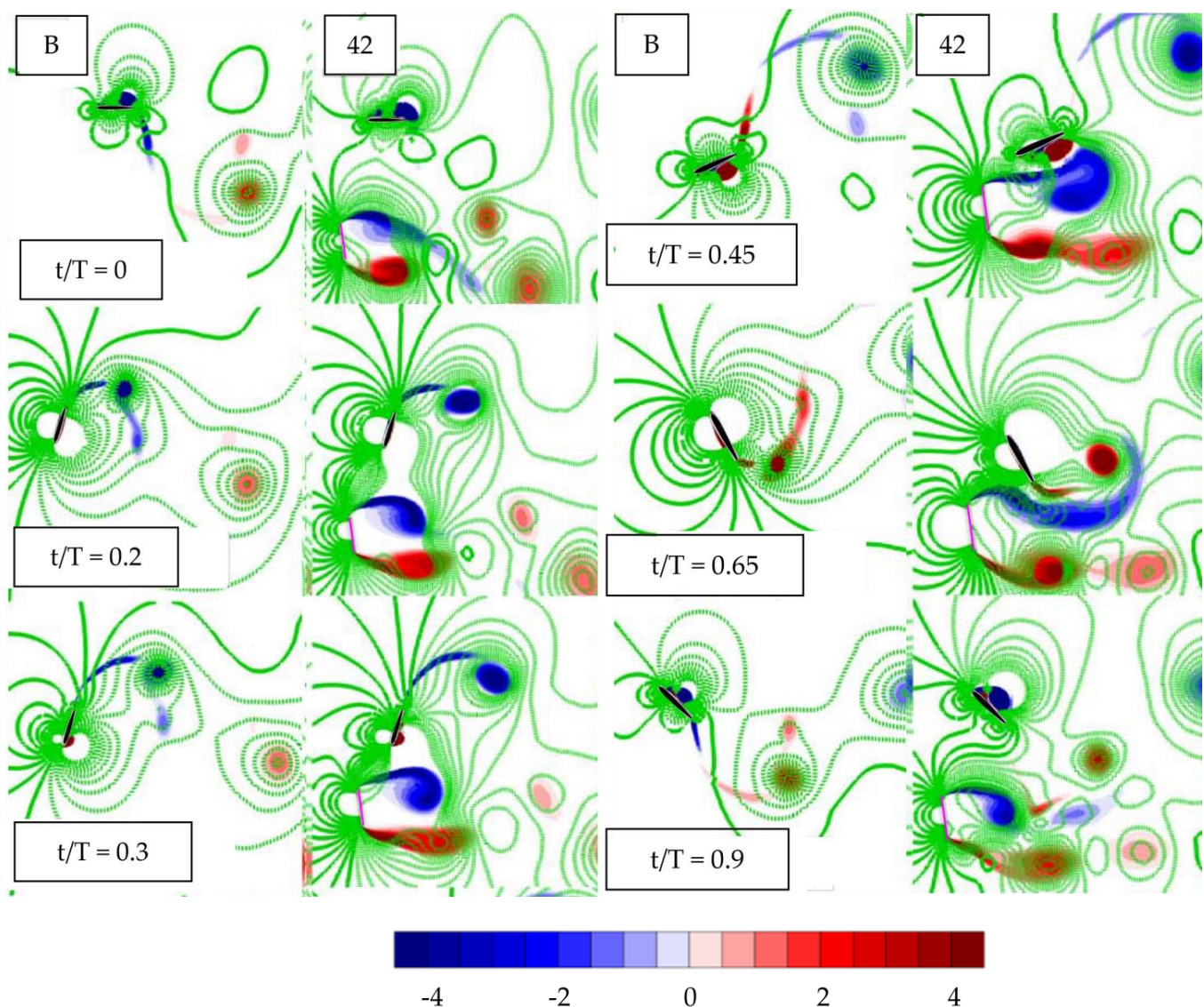


**Figure 6.** A comparison of the vortex structures and surface pressure distribution between the upstream-deflector hydrofoil and the conventional hydrofoil (solid isolines: positive pressure; dashed isolines: negative pressure).

The distribution of static pressure along the chord in Figure 7 was plotted at the middle of the downstroke ($t/T = 0.2$). At this instant, both upstream-deflector hydrofoil and conventional hydrofoil registered their highest instantaneous power coefficients. In the case of an upstream-deflector hydrofoil, the differential pressure between the upper and lower surfaces in Figure 7 increased sharply as compared to the baseline hydrofoil.

Although the upstream deflector barely altered the hydrofoil's top surface pressure, there was a substantial change in the pressure below the surface, which increased the negative lift force and heave power. Observations of the vortex structures in Figure 6 revealed that one pair (1P) of vortices is shed from the leading edge (LE) of the hydrofoil over the first half-cycle, and the same characteristic repeats in the next half-cycle. The presence of a deflector could strengthen the newly formed attached LEV on the hydrofoil's lower surface throughout the course of its development in both downstroke and upstroke. These vortices continue to grow until the hydrofoil attains peak angle of attack at mid stroke and then eventually detach due to the flow separation mechanism (see Figures 5 and 6; $t/T = 0.2$ and 0.65). Meanwhile, the hydrofoil's lift force and heave power increased significantly at $t/T = 0.65$ when a portion of the von Kármán vortex shed from the deflector interacted constructively with the hydrofoil's vortices (formed at the start of the upstroke). The amount of lift force created by the hydrofoil's motion was crucial to the power extraction process. Factors of the upstream deflector, such as the geometry and position, affected the hydrofoil's lift and power extraction. The deflector produced a deflected flow (from the top and bottom edges) much faster than the free-stream velocity and a recirculation flow of low velocity behind it. As this deflected flow impinged on the hydrofoil, it modified its effective angle of attack, increasing the lift force and, eventually, power extraction.
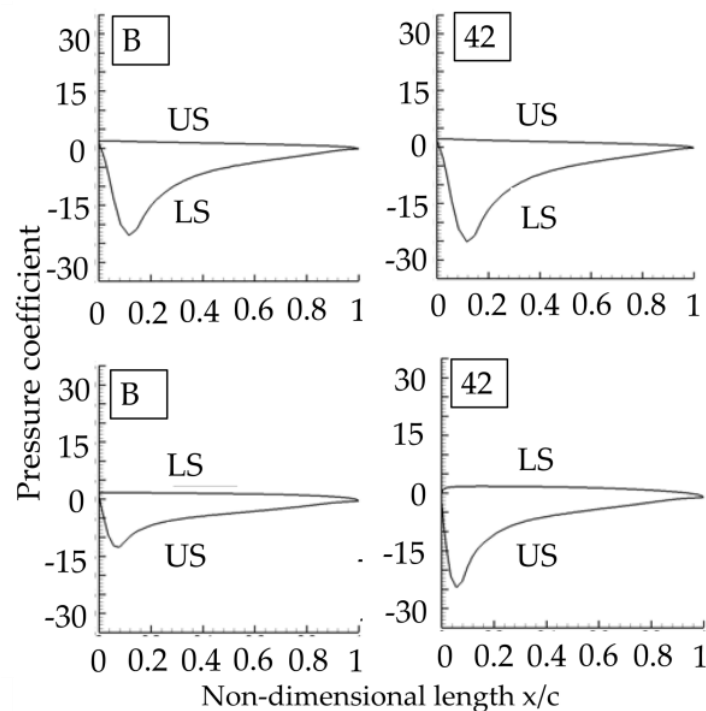


**Figure 7.** A comparison of the surface pressure distribution between the upstream-deflector hydrofoil and the conventional hydrofoil (first row: $t/T = 0.2$; second row: $t/T = 0.65$).

### 3.3. Effect of Number of Upstream Deflectors N on the Hydrofoil's Performance

The role of the upstream deflector $N$ on the cycle-averaged lift and power extracted by an oscillating hydrofoil with a pitch amplitude of $\theta_o = 76°$ and a reduced frequency of $f^* = 0.14$ was discussed previously in Figure 4. In this study, the hydrofoil's performance under single ($N = 1$) and dual ($N = 2$) upstream deflector designs was evaluated and compared with the "no deflector" situation. Here, a single or dual deflector was placed vertically (tilt angle $\beta = 0°$) in all three of the cases considered for analysis. The instantaneous $C_L$, $C_{PY}$, $C_{P\theta}$, and $C_P$ of an oscillating hydrofoil with a single/dual upstream deflector design were compared with the baseline in Figure 8. The details of case 18 were as follows: $N = 1$, $I_1{}^* = 1$, $J_1{}^* = 1/2$, and $\beta = 0°$. The details of case 27 were as follows: $N = 2$, $I_1{}^* = 1$, $I_2{}^* = 1$, $J_1{}^* = 1/2$, $J_2{}^* = 1/2$, and $\beta = 0°$. The details of case 35 are as follows: $N = 2$, $I_1{}^* = 1$, $I_2{}^* = 1$, $J_1{}^* = 1/2$,

$J_2^* = 1$, and $\beta = 0°$. Here, subscript 1 represents the bottom deflector, and 2 represents the top deflector. The heave power coefficient $C_{PY}$ remained mostly positive throughout the cycle due to perfect synchronization between the instantaneous lift coefficient $C_L$ and the heave velocity $V_Y$. The time history of $C_L$ in Figure 8a and $C_{PY}$ in Figure 8b revealed that the upstream deflector's presence was conducive to improving the heave power of the oscillating hydrofoil by increasing the lift force for most of the cycle. However, the amount of lift force increment and the timing of peak lift will largely depend on the upstream deflector's design and position. Meanwhile, during wing reversal (supination and pronation), the presence of a deflector will lead to poor synchronization between the lift coefficient $C_L$ of the hydrofoil and the heave velocity $V_Y$, leading to a deterioration in the heave power extraction. The pitch power coefficient $C_{P\theta}$, on the other hand, increased during pronation but decreased during supination when a deflector was present (see Figure 8c).
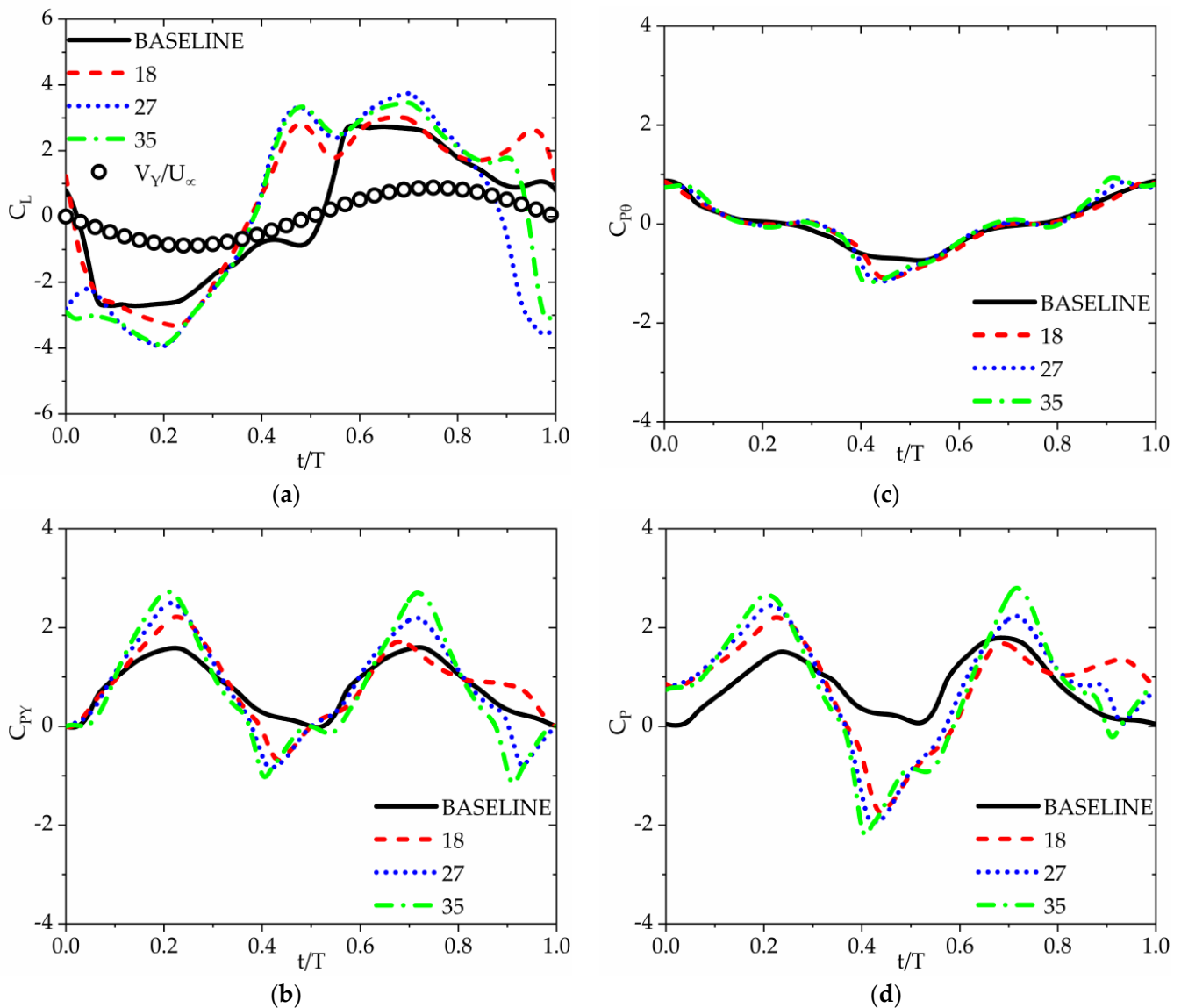


**Figure 8.** A comparison of the instantaneous lift and power coefficients of an oscillating hydrofoil equipped with a single/dual upstream deflector. (**a**) Lift coefficient. (**b**) Heave power coefficient. (**c**) Pitch power coefficient. (**d**) Net power coefficient.

Finally, the flow field of the considered cases 18, 27 and 35 was analyzed at six different time instants to reveal the mechanism responsible for the improvement in power extraction. Figures 9 and 10 compare the vortex structure evolution in a single cycle between the

upstream-deflector hydrofoil and the baseline hydrofoil (B). In case 18 (single-deflector hydrofoil), as the hydrofoil translated down ($t/T = 0.2–0.3$), the LEV attached to the lower surface of the upstream-deflector hydrofoil was more robust than the LEV of the baseline hydrofoil, delaying the flow separation (refer to Figure 9). Meanwhile, a portion of von Kármán vortex shed by the bottom deflector induced a high-velocity flow near the leading edge of the hydrofoil, causing an increase in the effective angle of attack and lift force (see Figure 11). This effect could assist case 18 (single-deflector hydrofoil) in generating more negative lift force and power than the baseline hydrofoil, as shown in Figure 8. Contrarily, in cases 27 and 35 (dual-deflector hydrofoil), the top upstream deflector could have a detrimental impact on the hydrofoil's lift and power extraction at $t/T = 0$ (start of downstroke). Before the beginning of the downstroke (at $t/T = 0.9$), a significant flow separation was observed behind the dual-deflector hydrofoils, possibly due to the presence of a second deflector at the top (refer to Figure 10).
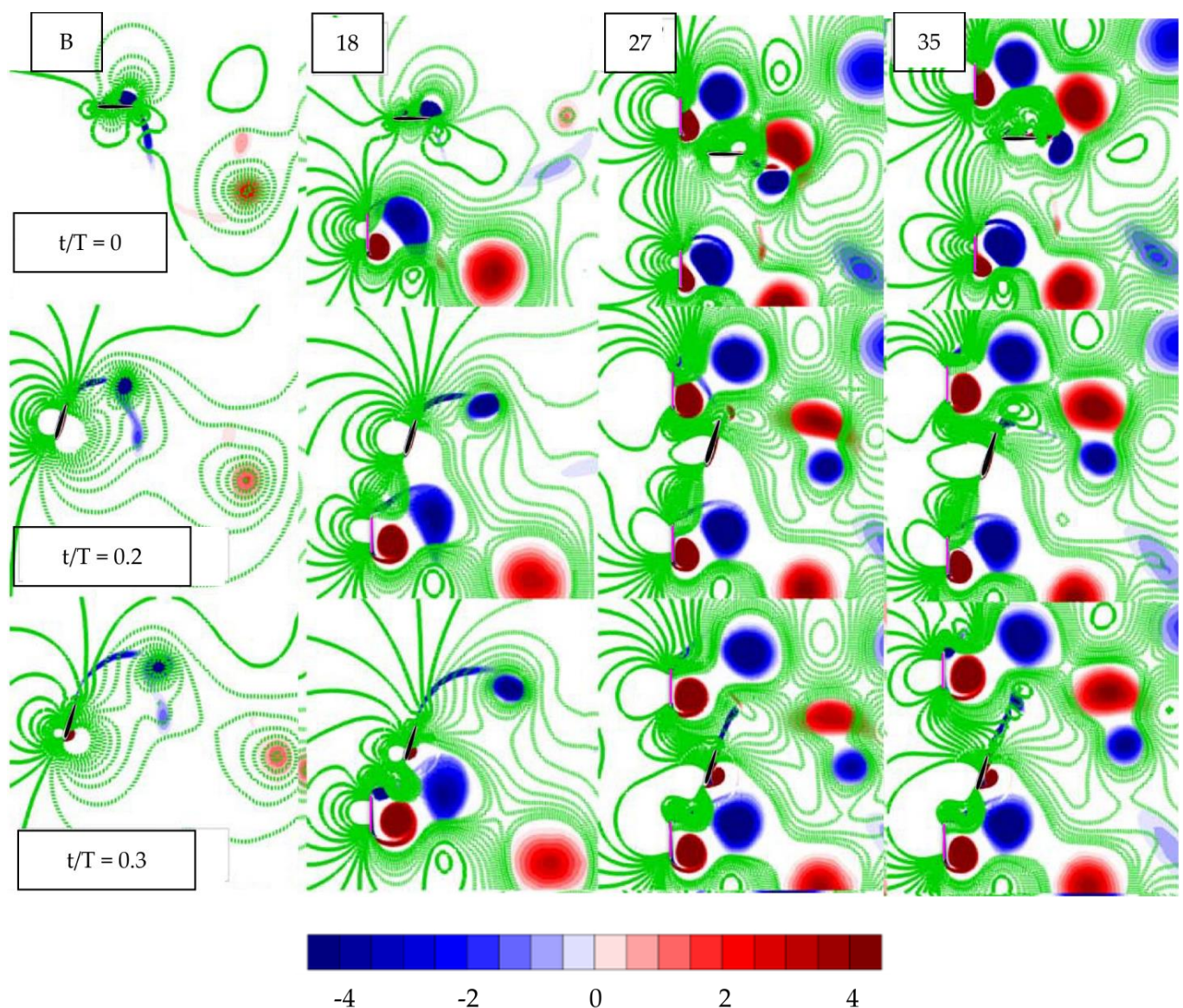


**Figure 9.** A comparison of the vortex structures and isolines of pressure of an oscillating hydrofoil equipped with a single/dual upstream deflector during downstroke (solid isolines: positive pressure; dashed isolines: negative pressure).
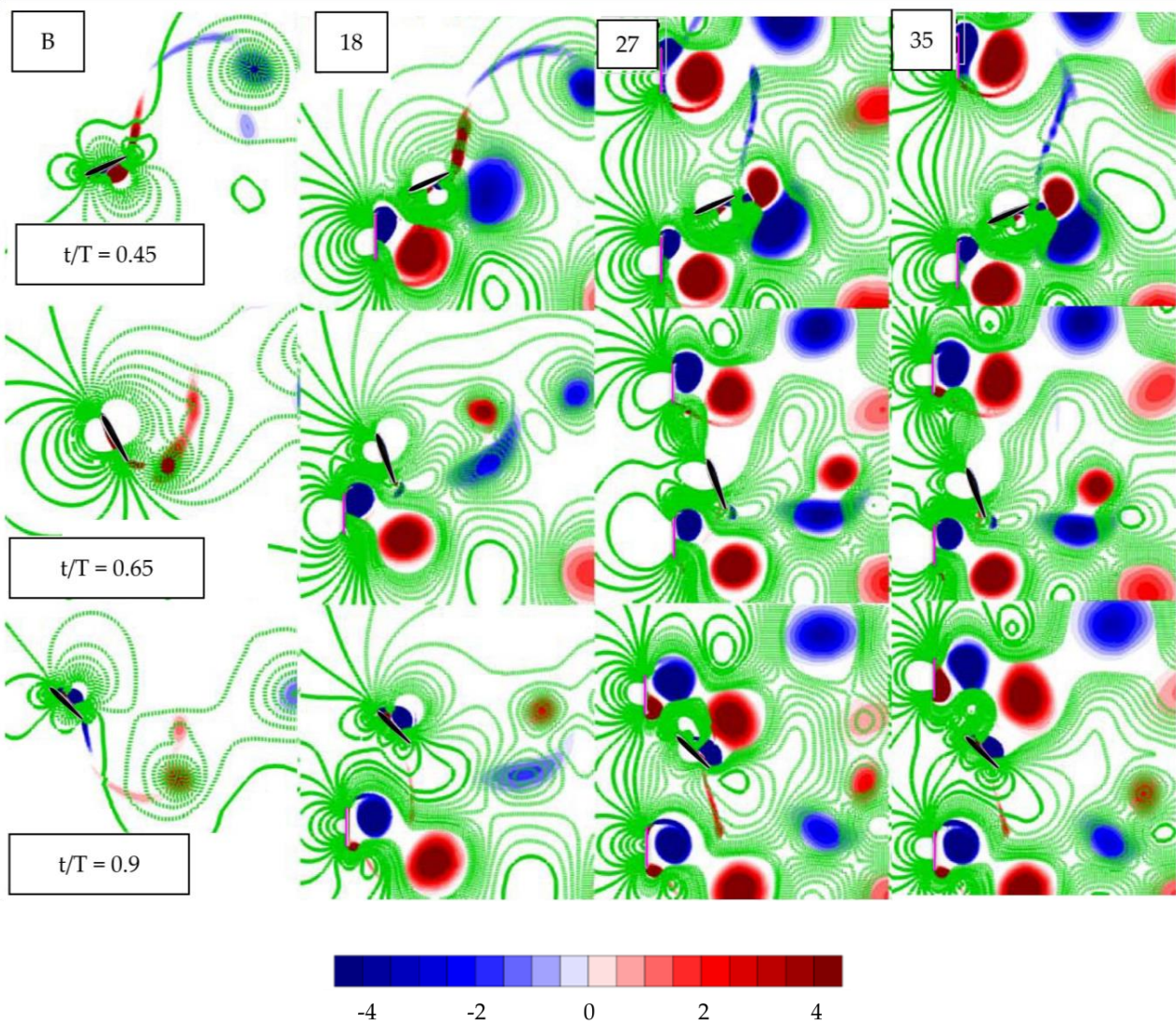
**Figure 10.** A comparison of the vortex structures and isolines of pressure of an oscillating hydrofoil equipped with a single/dual upstream deflector during upstroke. (solid isolines: positive pressure; dashed isolines: negative pressure).
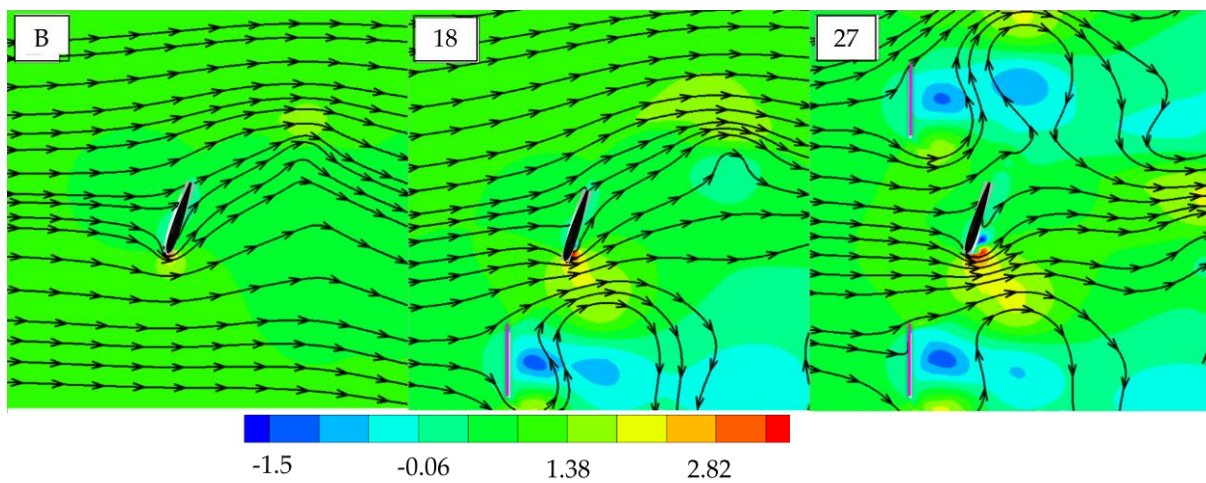


**Figure 11.** A comparison of the streamwise velocity and streamlines of an oscillating hydrofoil equipped with a single/dual upstream deflector.

For the dual upstream deflector design (cases 27 and 35), the LEV attached to the hydrofoil's lower surface was much more robust, further delaying the onset of flow separation. The negative lift force and power were further increased as the dual deflector amplified the deflected flow's velocity to peak before impinging on the hydrofoil's leading edge, as shown in Figure 11. This indicates that the dual deflector design was more effective than others. During the supination phase of the cycle, the oscillating hydrofoil was close to the upstream deflector (located at the bottom), resulting in a decrease in the lift force and a corresponding decrease in the power extracted by the hydrofoil. Meanwhile, the dual deflector design was seen to be even more detrimental to power extraction as compared to others. As the hydrofoil translated up, the power extraction of the dual-deflector hydrofoil (cases 27 and 35) was superior to that of the baseline hydrofoil. Conversely, the power extracted by a single-deflector hydrofoil (case 18) was the same as that of the baseline hydrofoil. This clearly indicates that a dual deflector design can be more beneficial than a single deflector for certain deflector positions.

The surface pressure distributions around the single/dual deflector hydrofoil and the baseline hydrofoil are compared in Figure 12. During the downstroke, the hydrofoil's lower surface (LS) was the suction side, while the upper surface (US) was the pressure side. Case 18 (single-deflector hydrofoil design) generated more (negative) lift force and power coefficient than the baseline hydrofoil due to an increase in surface pressure difference attributable to the deflector. Cases 27 and 35 (dual-deflector hydrofoil design) exhibited a much larger differential pressure, resulting in superior power extraction performance. Meanwhile, in the upstroke, the hydrofoil's lower surface (LS) was the pressure side, while the upper surface (US) was the suction side. The deflector had a role similar to that of the downstroke in terms of the hydrofoil's differential surface pressure.
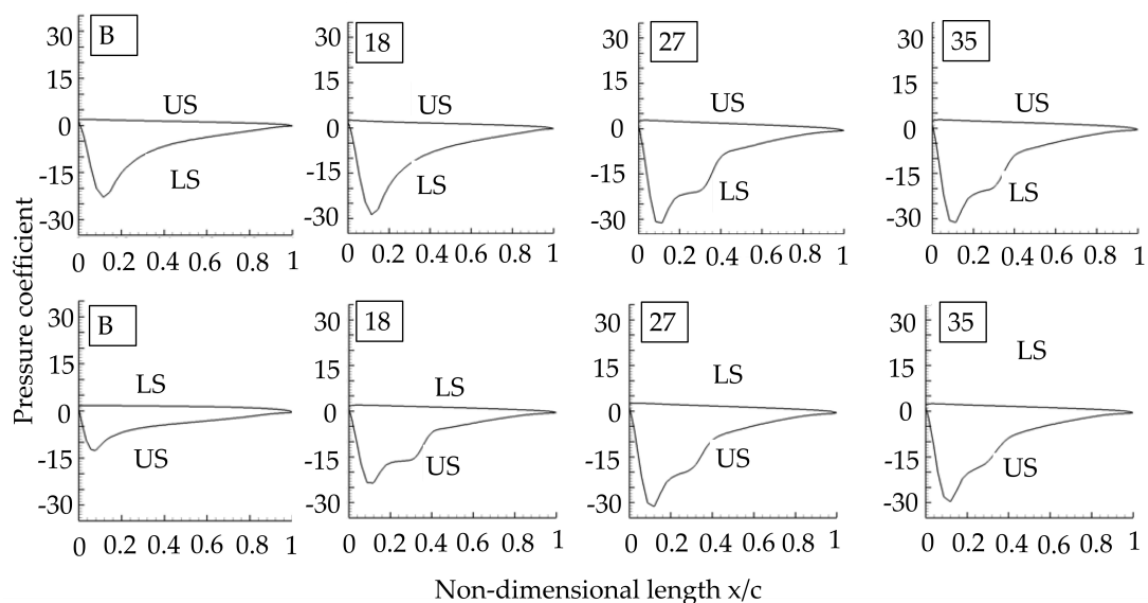


**Figure 12.** A comparison of the pressure distribution around the oscillating hydrofoil with a single/dual upstream deflector (upper surface (US) and lower surface (LS)) (First row: $t/T = 0.2$; second row: $t/T = 0.65$).

### 3.4. Effect of Deflector-Hydrofoil Spacing J* on the Hydrofoil's Performance

The instantaneous $C_L$, $C_{PY}$, $C_{P\theta}$, and $C_P$ of a hydrofoil with a single upstream deflector at three different vertical spacings J* are shown in Figure 13. The details of case 3 are as follows: $N = 1$, $I_1{}^* = 1$, $J_1{}^* = 1/4$, and $\beta = -5°$. The details of case 20 are as follows: $N = 1$, $I_1{}^* = 1$, $J_1{}^* = 1/2$, and $\beta = -5°$. The details of case 41 are as follows: $N = 1$, $I_1{}^* = 1$, $J_1{}^* = 3/4$, and $\beta = -5°$. Here, subscript 1 represents the bottom deflector. Cases 3, 20, and 41 had a single deflector placed at a tilt angle of $-5°$ with a corresponding vertical

spacing $J^*$ of 1/4, 1/2, and 3/4, respectively. In the downstroke, the peak lift coefficient $C_L$ (negative value) and power coefficient $C_P$ of the upstream-deflector hydrofoil were higher than those of the baseline hydrofoil. In case 3 ($J^* = 1/4$), the deflector was relatively close to the hydrofoil, causing the largest peaks in $C_L$ (negative value) in Figure 13a and $C_P$ in Figure 13d as compared to the other cases, but these quickly dropped after the peaks. Since the upstream deflector could be destructive for the hydrofoil in its supination phase, the power extraction by the hydrofoil was poorer than without the deflector.
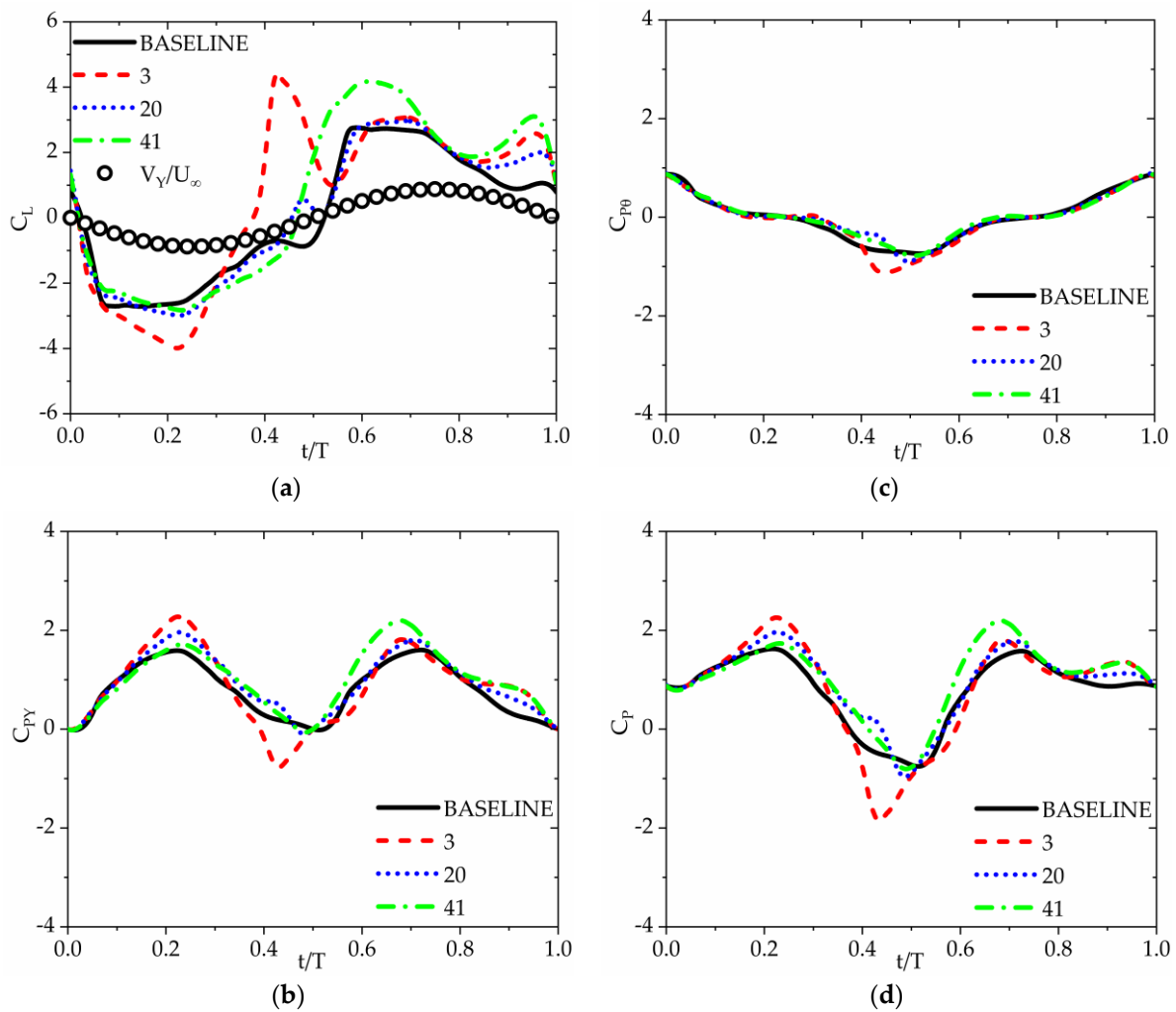


**Figure 13.** A comparison of the instantaneous lift and power coefficients of a hydrofoil with an upstream deflector at different values of deflector–hydrofoil spacing $J^*$. (**a**) Lift coefficient. (**b**) Heave power coefficient. (**c**) Pitch power coefficient. (**d**) Net power coefficient.

As shown in Figure 13, the performance of the hydrofoil with the upstream deflector was subpar with the baseline in the time interval $t/T = 0.3$–$0.6$. However, after supination, the upstream-deflector hydrofoil performed at par with the baseline hydrofoil during the upstroke's translation phase. Case 20 ($J^* = 1/2$), in which the deflector was placed further away from the hydrofoil, showed a slight improvement in the hydrofoil's performance in both strokes. For case 41 ($J^* = 3/4$), the deflector's constructive effect on the hydrofoil's performance was minimal during the downstroke but substantial during the upstroke.

The vortex structures, velocity streamlines, and surface pressure distributions around the hydrofoil at multiple instants with varying vertical spacing $J^*$ are depicted in Figures 14–17. When the hydrofoil reached the middle of the downstroke ($t/T = 0.2$–$0.3$), the upstream deflector of case 3 ($J^* = 1/4$) fully strengthened the leading edge vortex (LEV) on the hydrofoil's LS, and the vortex grew further due to the smaller deflector–hydrofoil

spacing, as shown in Figures 14 and 15. The streamlines in the deflector–hydrofoil spacing were largely skewed, causing a region of high velocity at the leading edge, which could affect the effective angle of attack of the hydrofoil (see Figure 16). Meanwhile, the hydrofoil's differential surface pressure, as shown in Figure 17, was significantly higher than that in other cases, resulting in a substantial lift and power coefficient. When the deflector was located further away, the skewness noticed in the streamlines at the deflector–hydrofoil spacing weakened, and the deflector's contribution to the flow enhancement became insignificant. In case 20, $J^*$ was increased to 1/2 and the LEV on the hydrofoil's LS was partially strengthened by the upstream deflector during downward translation ($t/T = 0.2$–0.3). As seen in Figure 17, the suction pressure at the hydrofoil's LS at $t/T = 0.2$ was marginally higher than that at the baseline. During the same interval ($t/T = 0.2$–0.3), the LEV on the LS was only poorly strengthened in case 41 ($J^* = 3/4$). As a result, the differential surface pressure in Figure 17 remained nearly unchanged as compared to the baseline.
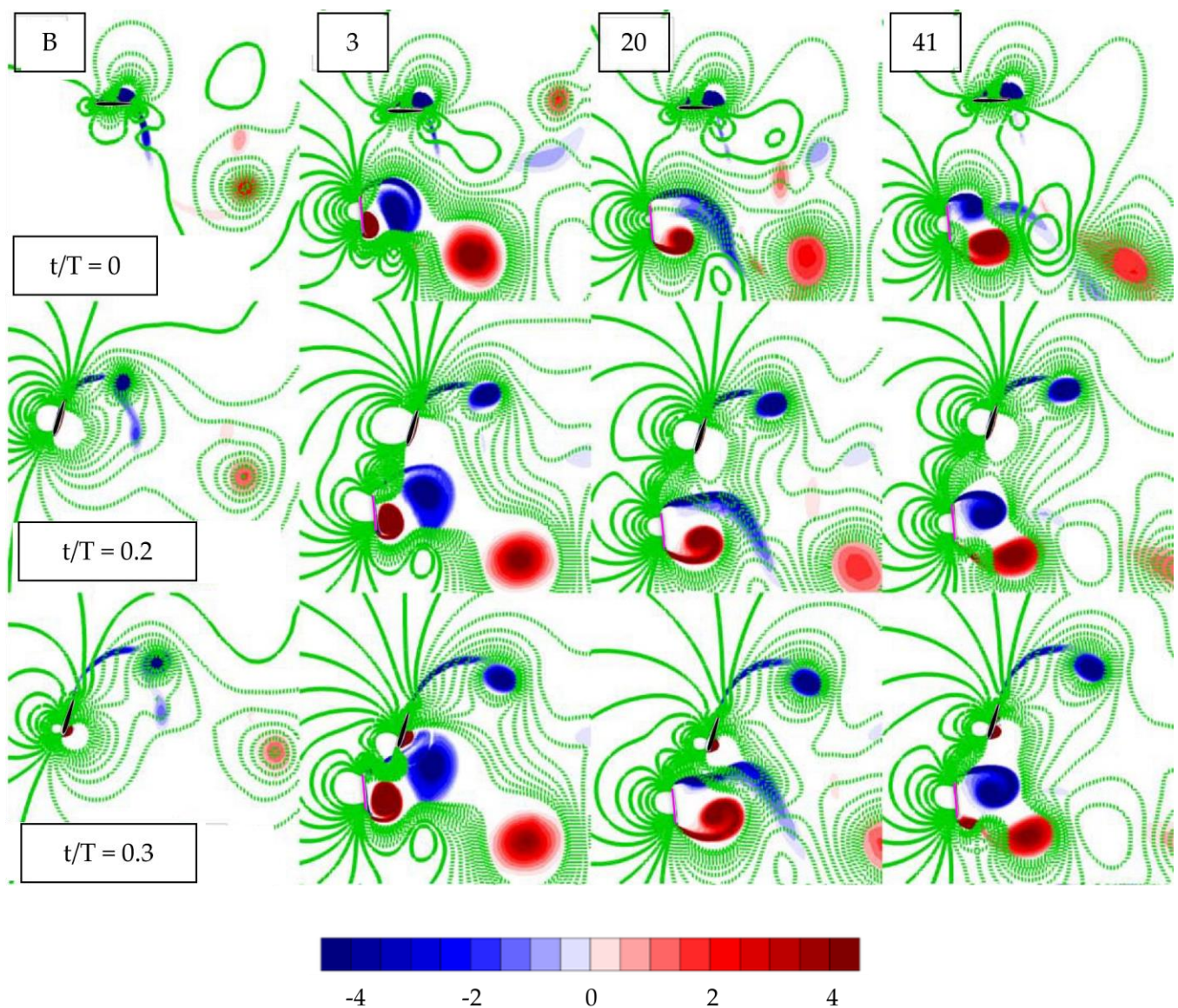


**Figure 14.** A comparison of the vortex structures and isolines of pressure of a hydrofoil with an upstream deflector at different deflector–hydrofoil spacings $J^*$ during downstroke (solid isolines: positive pressure; dashed isolines: negative pressure).
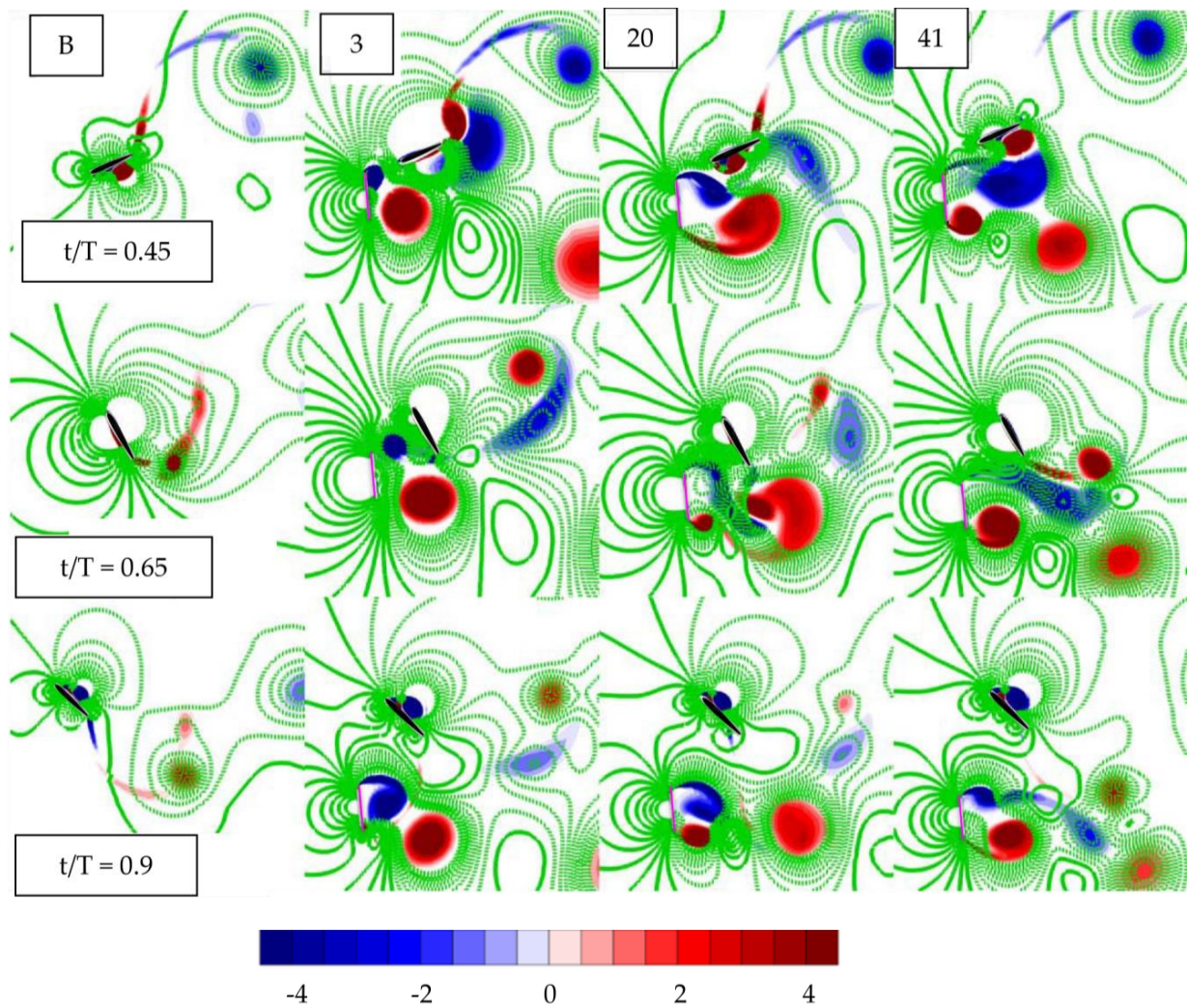
**Figure 15.** A comparison of the vortex structures and isolines of pressure of a hydrofoil with an upstream deflector at different deflector–hydrofoil spacings *J\** during upstroke (solid isolines: positive pressure; dashed isolines: negative pressure).
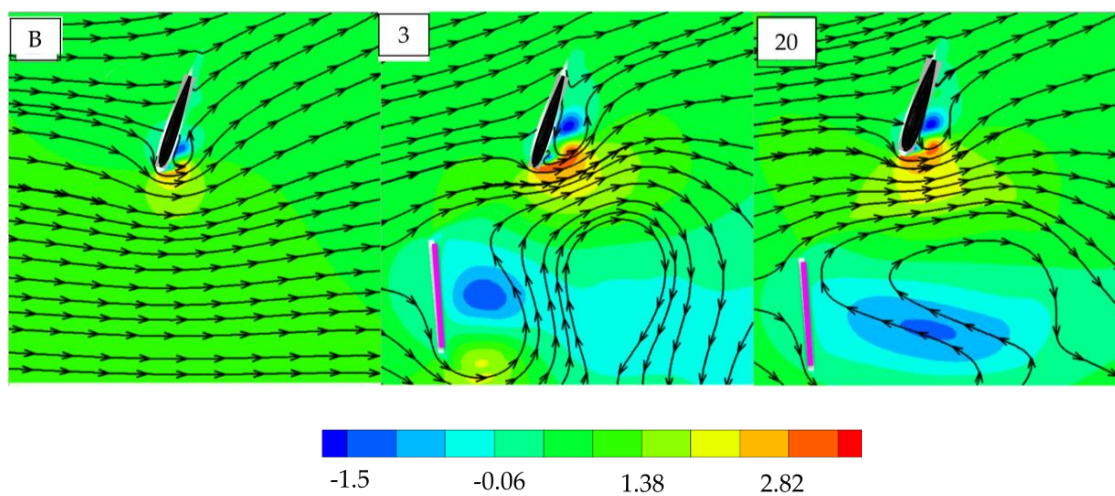


**Figure 16.** A comparison of the streamwise velocity and streamlines of a hydrofoil with an upstream deflector at different deflector–hydrofoil spacings *J\**.
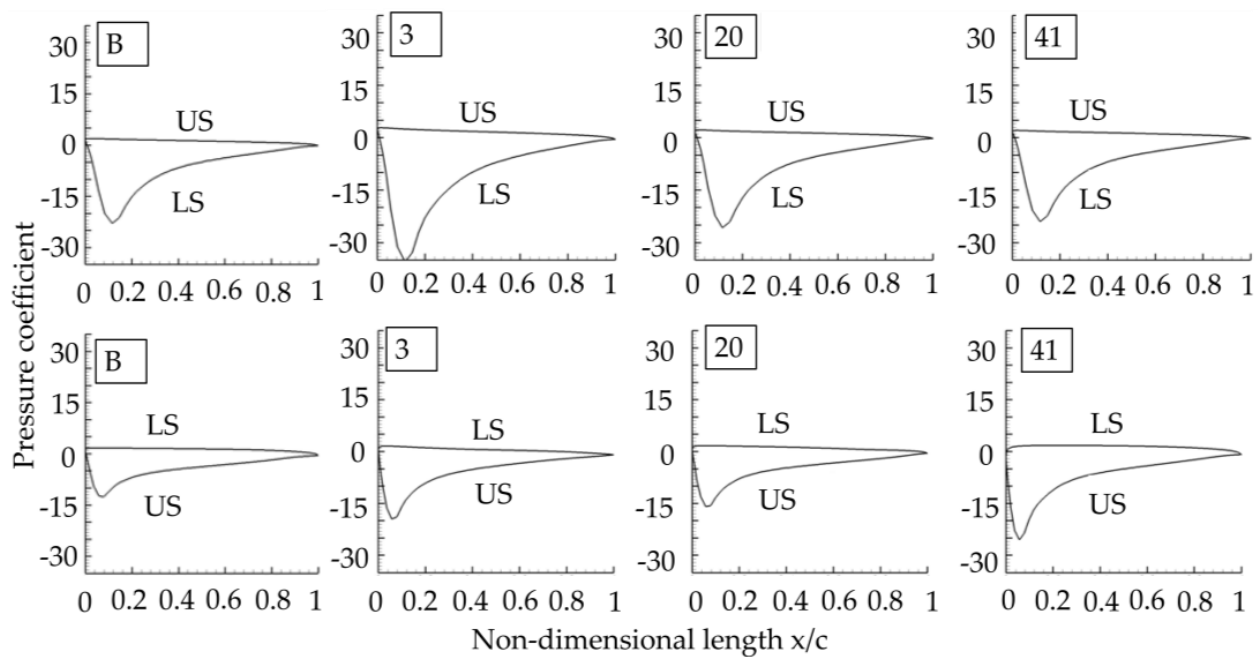
**Figure 17.** A comparison of pressure distributions around the oscillating hydrofoil with an upstream deflector at different deflector–hydrofoil spacings $J^*$ (upper surface (US) and lower surface (LS) (first row: $t/T = 0.2$; second row: $t/T = 0.65$).

During supination, case 3 ($J^* = 1/4$) suffered in terms of power coefficient due to premature flow separation on the hydrofoil's LS. Contrarily, cases 20 and 41 generated power at par with the baseline due to a slight delay in the flow separation (see Figures 13–15). As the hydrofoil translated upwards, the LEV (on the US) in cases 3 and 20 was found to be marginally robust, while the LEV in case 41 was fully robust. Furthermore, the differential surface pressure around the hydrofoil shown in Figure 17 was significantly higher in case 41 than that in other cases, resulting in tremendous lift and power. One must remember that the hydrofoil's pitch motion facilitates a high positive angle of attack to the flow during the upstroke and hence, even a tiny change in the surface pressure can lead to a large variation in the lift force.

### 3.5. Effect of Tilt Angle β of the Upstream Deflector on the Hydrofoil's Performance

The effect of the upstream deflector on the power extraction performance of the oscillating hydrofoil was investigated for various tilt angles $\beta$. The tilt angle of the deflector considered in the present study was in the range $-60° \leq \beta \leq 70°$. The results revealed that the tilt angle $\beta$ of the upstream deflector had a huge impact on the power extraction performance of the oscillating hydrofoil, as shown in Figure 4. The rightward tilted upstream deflector at a low tilt angle ($-1° \leq \beta \leq -10°$) was observed to be more beneficial by significantly improving the power extraction efficiency $\eta$ of the oscillating hydrofoil (refer to Figure 4). Of particular importance, the maximum efficiency was recorded in case 42 when $\beta$ was $-7.5°$.

The instantaneous values of $C_L$, $C_{PY}$, $C_{P\theta}$, and $C_P$ for different tilt angles (cases 40, 42 and 52) at a vertical spacing $J^*$ of 3/4 are plotted in Figure 18. In the three cases presented (40, 42 and 52), the hydrofoil was equipped with a single upstream deflector at a tilt angle $\beta$ of $-4°$, $-7.5°$, and $10°$, respectively. The details of case 40 are as follows: $N = 1$, $I_1^* = 1$, $J_1^* = 3/4$, and $\beta = -4°$. The details of case 42 are as follows: $N = 1$, $I_1^* = 1$, $J_1^* = 3/4$, and $\beta = -7.5°$. The details of case 52 are as follows: $N = 1$, $I_1^* = 1$, $J_1^* = 3/4$, and $\beta = 10°$. Here, subscript 1 represented the bottom deflector. The positive tilt angle represented the leftward tilt, and the negative tilt angle represented the rightward tilt. Cases 40 and 42 corresponded to the hydrofoil equipped with a rightward tilted upstream deflector, while

case 52 corresponded to the hydrofoil equipped with a leftward tilted upstream deflector. The vortex structures in Figures 19 and 20 revealed that the upstream deflector at a low tilt angle shed vortex obliquely relative to it. As the hydrofoil translated down ($t/T = 0.3$), the shear layers detached from the upper edge of the upstream deflector roll to form a vortex, which was then located underneath the hydrofoil. The upstream deflector at a low tilt angle, irrespective of the tilt direction (right or left), mildly strengthened the LEV on the LS of the hydrofoil, causing a noticeable improvement in the power coefficient as compared to the baseline (see Figures 18–20).
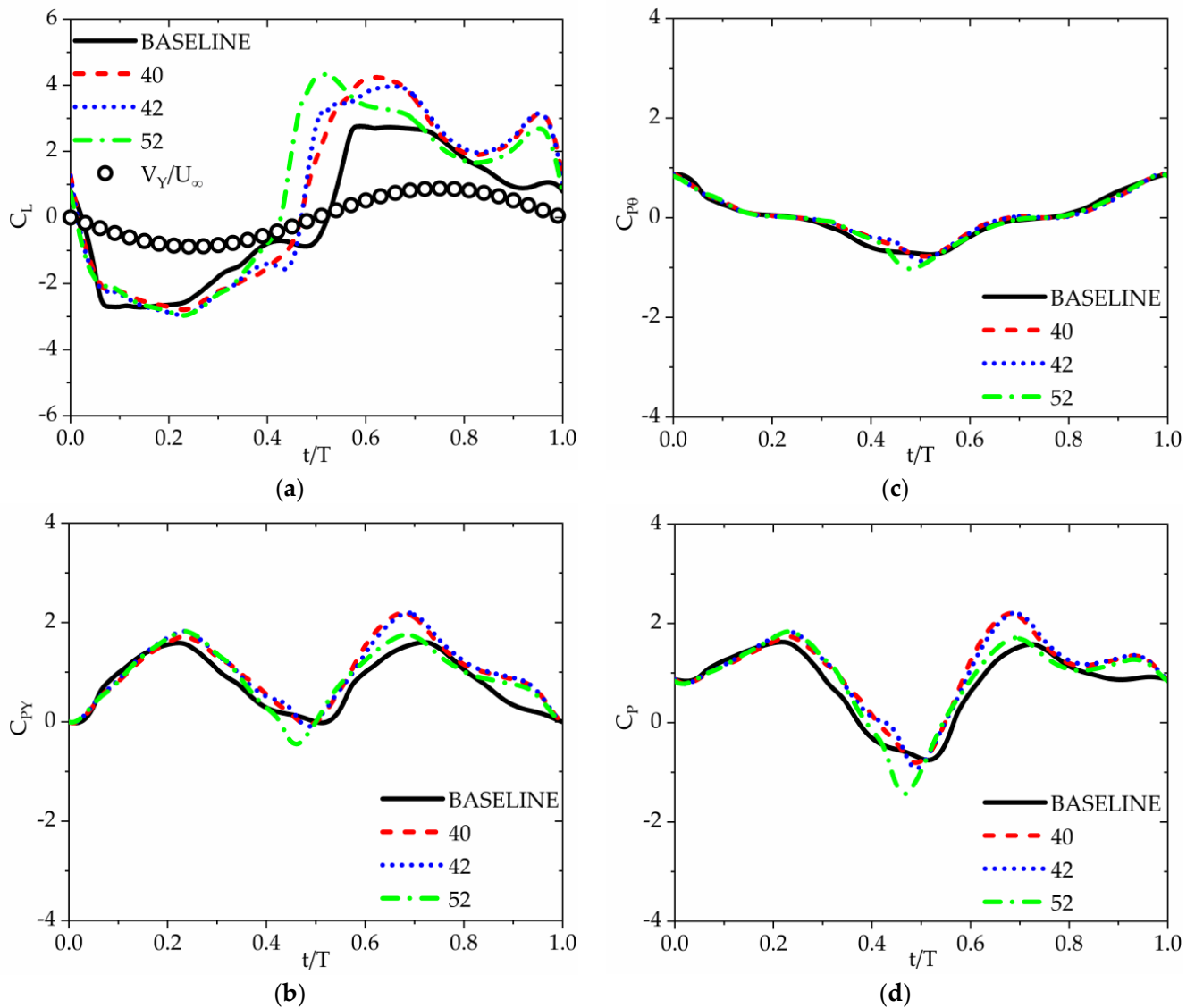


**Figure 18.** A comparison of the instantaneous lift and power coefficients of an oscillating hydrofoil with an upstream deflector with different tilt angles. (**a**) Lift coefficient. (**b**) Heave power coefficient. (**c**) Pitch power coefficient. (**d**) Net power coefficient.

Meanwhile, the surface pressure distribution shown in Figure 21 induced no noticeable changes in the pressure difference between the lower and the upper surfaces. In the supination phase, the hydrofoil equipped with the leftward tilted upstream deflector was more detrimental in terms of power extraction performance as compared to the hydrofoil equipped with the rightward tilted upstream deflector and baseline (see Figure 18d). This was one of the reasons behind the better net power coefficient observed in the hydrofoil equipped with the rightward tilted upstream deflector. As the hydrofoil translated up

($t/T$ = 0.65), the LEV on the US of the hydrofoil grew faster by absorbing additional flow energy deflected from the upstream deflector in supination. The rightward tilted upstream deflector at a low tilt angle strengthened the LEV on the US of the hydrofoil, as shown in Figure 20, causing a significant improvement in the power coefficient as compared to the baseline (see Figure 18d). However, if the upstream deflector was tilted leftward, this would induce unnecessary loss of power on the suction side of the hydrofoil as compared to the rightward tilted upstream deflector. Meanwhile, the surface pressure distribution in Figure 21 revealed that the pressure difference between the upper and lower surfaces was significantly higher for the hydrofoil equipped with the rightward tilted upstream deflector as compared to the baseline. This explains why the positive lift was larger in cases 40 and 42 as compared to the baseline, eventually generating more heave power (see Figure 18a,d).
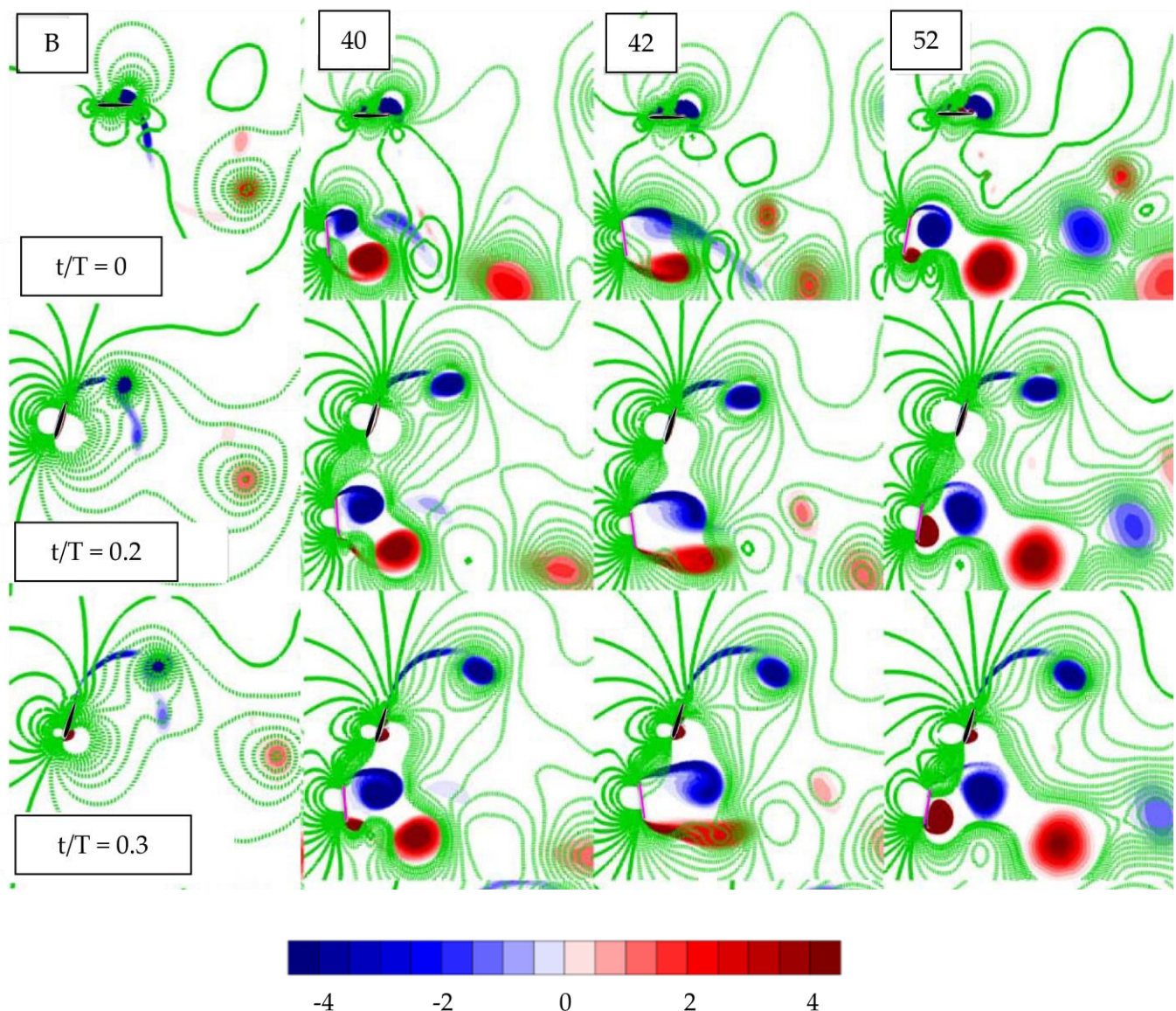


**Figure 19.** A comparison of the vortex structures and isolines of pressure of an oscillating hydrofoil for different tilt angles of the upstream deflector during downstroke (solid isolines: positive pressure; dashed isolines: negative pressure).
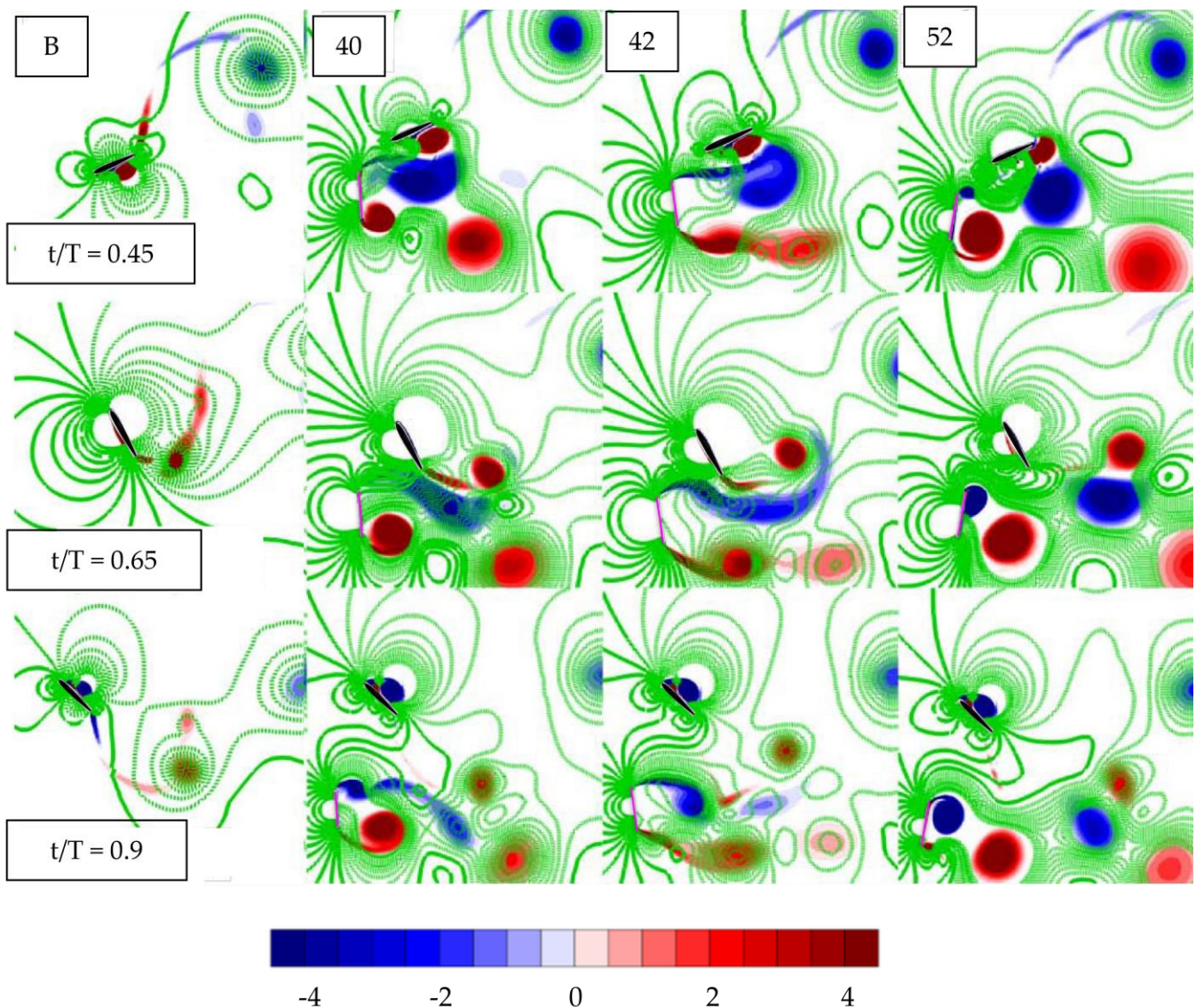
**Figure 20.** A comparison of the vortex structures and isolines of pressure of an oscillating hydrofoil for different tilt angles of the upstream deflector during upstroke (solid isolines: positive pressure; dashed isolines: negative pressure).

The relation between the power extracted by the hydrofoil and the flow field is quantified in Table 3. It can be seen from the data that one pair (1P) of the vortex was formed in each stroke. The LEV played a vital role in power generation in all nine cases presented in the analysis section. The power extracted by the hydrofoil was largely dependent on the strength and robustness of LEV. The deflector–hydrofoil vortex interaction was another key mechanism that affected power extraction. The type of deflector–hydrofoil vortex interaction observed in each phase of a cycle is categorically specified in Table 3. Two types of deflector–hydrofoil vortex interaction were observed, namely, constructive and destructive, which affected the power extraction differently.
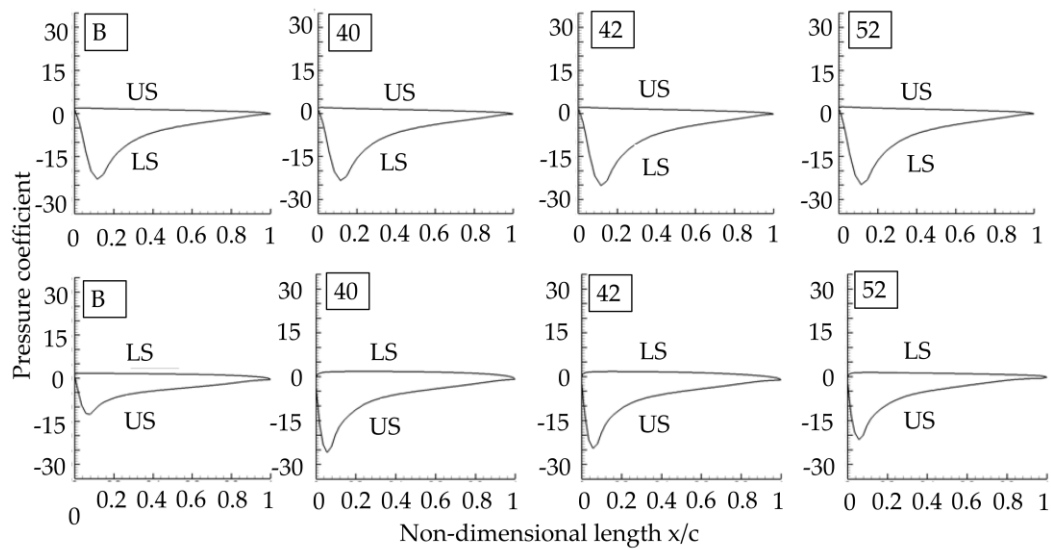
**Figure 21.** Comparison of surface pressure coefficient on the upper surface (US) and lower surface (LS) around the oscillating hydrofoil for different tilt angles of the upstream deflector (first row: $t/T = 0.2$; second row: $t/T = 0.65$).

**Table 3.** Relationship between $C_P$ and flow field for the nine analyzed cases (R: Reduced, I: Increased, C: Constructive, D: Destructive, X: No effect; tick mark represents the existence of vortex).

| Case | N | $J_1$ * | $J_2$ * | $\beta_1$ * | $\beta_2$ * | $\dfrac{\bar{C_P}}{\bar{C_{P,b}}}$ | Vortex Type | | Role of Deflector–Hydrofoil Vortex Interaction | | | |
|---|---|---|---|---|---|---|---|---|---|---|---|---|
| | | | | | | | 1P | LEV | Pronation | Down | Up | Supination |
| 18 | 1 | 1/2 | | 0 | | R | ✓ | ✓ | C | C | X | D |
| 27 | 2 | 1/2 | 1/2 | 0 | 0 | I | ✓ | ✓ | D | C | C | D |
| 35 | 2 | 1/2 | 1 | 0 | 0 | I | ✓ | ✓ | D | C | C | D |
| 3 | 1 | 1/4 | | −5 | | I | ✓ | ✓ | C | C | X | D |
| 20 | 1 | 1/2 | | −5 | | R | ✓ | ✓ | D | C | X | X |
| 41 | 1 | 3/4 | | −5 | | I | ✓ | ✓ | C | X | C | X |
| 40 | 1 | 3/4 | | −4 | | I | ✓ | ✓ | C | X | C | X |
| 42 | 1 | 3/4 | | −7.5 | | I | ✓ | ✓ | C | X | C | X |
| 52 | 1 | 3/4 | | 10 | | I | ✓ | ✓ | C | X | X | D |

## 4. Conclusions

In this study, we used numerical simulations to investigate the effect of positional parameters of an upstream deflector on the power extraction performance of an oscillating hydrofoil turbine. The flow field and instantaneous power extracted from the hydrofoil were also examined as it oscillated. The numerical and mesh models were compared with results in the current literature, and a good match was established. The upstream deflector was found to greatly increase the lift force and power extraction by acting as a flow augmentation device. The performance of the oscillating hydrofoil was computed by varying parameters such as the number of upstream deflectors $N$, tilt angle of the upstream deflector $\beta$, and deflector–hydrofoil spacing $J^*$. Simulation results revealed that the efficiency $\eta$ was heavily dependent on all three aforementioned parameters. When the deflector was installed at its ideal position, the power coefficient $C_P$ of the oscillating hydrofoil was maximized due to the augmented flow, increasing the efficiency. The maximum power extraction efficiency of the hydrofoil was obtained when a single upstream deflector ($N = 1$) of height $L^* = 1$ was placed below the hydrofoil at $I^* = 1$, $J^* = 3/4$, and $\beta = -7.5°$. This maximum efficiency was nearly 32% higher than that of the baseline. The optimal ranges

of positional parameters were observed for $3/4 \leq J^* \leq 1$ and $-1° \geq \beta \geq -7.5$. The vortex structures revealed that the flow evolution and power extraction performance were indeed affected by the robustness, size, and growth of the LEV and the timing of LEV separation. To maximize the power extracted from an oscillating hydrofoil, one must understand the mechanism of vortex interaction between the deflector and the hydrofoil. Stronger vortex cores shed by the deflector interacting with the hydrofoil were advantageous in the midst of the downstroke and upstroke, but counterproductive in the latter half of the stroke. Further, the flow diverted by the upstream deflector had a much higher velocity when impinging on the hydrofoil, which could affect its effective angle of attack. Finally, numerical simulation results showed that a low-cost upstream deflector could greatly increase the power coefficient of an oscillating hydrofoil. The findings of this research have the potential to advance the development of a practical oscillating wing-based tidal device for power extraction.

**Data Availability Statement:** The data presented in this study are available on request from the corresponding author.

**Conflicts of Interest:** The authors declare no conflict of interest.

## References

1. Rogelj, J.; Den Elzen, M.; Höhne, N.; Fransen, T.; Fekete, H.; Winkler, H.; Schaeffer, R.; Sha, F.; Riahi, K.; Meinshausen, M. Paris Agreement climate proposals need a boost to keep warming well below 2 C. *Nature* **2016**, *534*, 631–639. [CrossRef] [PubMed]
2. Badescu, V.; Lazaroiu, G.C.; Barelli, L. *Power Engineering: Advances and Challenges Part B: Electrical Power*; CRC Press: Boca Raton, FL, USA, 2018; p. 436.
3. Bhatia, S.C. *Advanced Renewable Energy Systems (Part 1 and 2)*, 1st ed.; WPI Publishing: New Delhi, India, 2014; p. 775.
4. Ribeiro, B.L.R.; Frank, S.L.; Franck, J.A. High Reynolds Number Effects of an Oscillating Hydrofoil for Energy Harvesting. *arXiv* **2018**, arXiv:1802.05328.
5. Xiao, Q.; Zhu, Q. A review on flow energy harvesters based on flapping foils. *J. Fluids Struct.* **2014**, *46*, 174–191. [CrossRef]
6. Young, J.; Lai, J.C.; Platzer, M.F. A review of progress and challenges in flapping foil power generation. *Prog. Aerosp. Sci.* **2014**, *67*, 2–28. [CrossRef]
7. Kinsey, T.; Dumas, G. Parametric study of an oscillating airfoil in a power extraction regime. *AIAA J.* **2008**, *46*, 1318–1330. [CrossRef]
8. Zhu, Q. Optimal frequency for flow energy harvesting of a flapping foil. *J. Fluid Mech.* **2011**, *675*, 495–517. [CrossRef]
9. Wang, Y.; Sun, X.; Huang, D.; Zheng, Z. Numerical investigation on energy extraction of flapping hydrofoils with different series foil shapes. *Energy* **2016**, *112*, 1153–1168. [CrossRef]
10. Xiao, Q.; Liao, W.; Yang, S.; Peng, Y. How motion trajectory affects energy extraction performance of a biomimic energy generator with an oscillating foil? *Renew. Energy* **2012**, *37*, 61–75. [CrossRef]
11. Lu, K.; Xie, Y.; Zhang, D. Non sinusoidal motion effects on energy extraction performance of a flapping foil. *Renew. Energy* **2014**, *64*, 283–293. [CrossRef]
12. Lu, K.; Xie, Y.; Zhang, D.; Xie, G. Systematic investigation of the flow evolution and energy extraction performance of a flapping-airfoil power generator. *Energy* **2015**, *89*, 138–147. [CrossRef]
13. Veilleux, J.C.; Dumas, G. Numerical optimization of a fully-passive flapping-airfoil turbine. *J. Fluids Struct.* **2017**, *70*, 102–130. [CrossRef]
14. Ma, P.; Yang, Z.; Wang, Y.; Liu, H.; Xie, Y. Energy extraction and hydrodynamic behavior analysis by an oscillating hydrofoil device. *Renew. Energy* **2017**, *113*, 648–659. [CrossRef]
15. Sitorus, P.E.; Ko, J.H. Power extraction performance of three types of flapping hydrofoils at a Reynolds number of 1.7E6. *Renew. Energy* **2019**, *132*, 106–118. [CrossRef]
16. Kinsey, T.; Dumas, G. Optimal tandem configuration for oscillating-foils hydrokinetic turbine. *J. Fluid Eng.* **2012**, *134*, 031103. [CrossRef]

17. Picard-Deland, M.; Olivier, M.; Dumas, G.; Kinsey, T. Oscillating-foil turbine operating at large heaving amplitudes. *AIAA J.* **2019**, *57*, 5104–5113. [CrossRef]
18. Oshkai, P.; Iverson, D.; Lee, W.; Dumas, G. Reliability study of a fully-passive oscillating foil turbine operating in a periodically-perturbed inflow. *J. Fluids Struct.* **2022**, *113*, 103630. [CrossRef]
19. Xie, Y.H.; Jiang, W.; Lu, K.; Zhang, D. Numerical investigation into energy extraction of flapping airfoil with Gurney flaps. *Energy* **2016**, *109*, 694–702. [CrossRef]
20. Zhu, B.; Huang, Y.; Zhang, Y. Energy harvesting properties of a flapping wing with an adaptive Gurney flap. *Energy* **2018**, *152*, 119–128. [CrossRef]
21. Sun, G.; Wang, Y.; Xie, Y.; Lv, K.; Sheng, R. Research on the effect of a movable gurney flap on energy extraction of oscillating hydrofoil. *Energy* **2021**, *225*, 120206. [CrossRef]
22. Sun, G.; Wang, Y.; Xie, Y.; Ma, P.; Zhang, Y. Hydrodynamic and energy extraction properties of oscillating hydrofoils with a trailing edge flap. *Appl. Ocean Res.* **2021**, *110*, 102530. [CrossRef]
23. Zhou, D.; Cao, Y.; Sun, X. Numerical study on energy-extraction performance of a flapping hydrofoil with a trailing-edge flap. *Ocean Eng.* **2021**, *224*, 108756. [CrossRef]
24. Jiang, W.; Mei, Z.Y.; Wu, F.; Han, A.; Xie, Y.H.; Xie, D.M. Effect of shroud on the energy extraction performance of oscillating foil. *Energy* **2022**, *239*, 122387. [CrossRef]
25. Xu, B.; Ma, Q.; Huang, D. Research on energy harvesting properties of a diffuser-augmented flapping wing. *Renew. Energy* **2021**, *180*, 271–280. [CrossRef]
26. Dahmani, F.; Sohn, C.H. Effect of convergent duct geometry on the energy extraction performance of tandem oscillating hydrofoils system. *J. Fluids Struct.* **2020**, *95*, 102949. [CrossRef]
27. Le, T.Q.; Ko, J.H.; Byun, D. Morphological effect of a scallop shell on a flapping-type tidal stream generator. *Bioinspir. Biomim.* **2013**, *8*, 036009. [CrossRef] [PubMed]
28. Karbasian, H.R.; Esfahani, J.A.; Barati, E. Simulation of power extraction from tidal currents by flapping foil hydrokinetic turbines in tandem formation. *Renew. Energy* **2015**, *81*, 816–824. [CrossRef]
29. Zhu, J.; Tian, T. The time asymmetric pitching effects on the energy extraction performance of a semi-active flapping wing power generator. *Eur. J. Mech. B Fluids* **2017**, *66*, 92–101. [CrossRef]
30. Chen, Y.; Nan, J.; Wu, J. Wake effect on a semi-active flapping foil based energy harvester by a rotating foil. *Comput. Fluids* **2018**, *160*, 51–63. [CrossRef]
31. Teng, L.; Deng, J.; Pan, D.; Shao, X. Effects of non-sinusoidal pitching motion on energy extraction performance of a semi-active flapping foil. *Renew. Energy* **2016**, *85*, 810–818. [CrossRef]
32. Wong, K.H.; Chong, W.T.; Sukiman, N.L.; Shiah, Y.C.; Poh, S.C.; Sopian, K.; Wang, W.C. Experimental and simulation investigation into the effects of a flat plate deflector on vertical axis wind turbine. *Energy Convers. Manag.* **2018**, *160*, 109–125. [CrossRef]
33. Zhao, P.; Jiang, Y.; Liu, S.; Stoesser, T.; Zou, L.; Wang, K. Investigation of fundamental mechanism leading to the performance improvement of vertical axis wind turbines by deflector. *Energy Convers. Manag.* **2021**, *247*, 114680. [CrossRef]
34. Golecha, K.; Eldho, T.I.; Prabhu, S.V. Influence of the deflector plate on the performance of modified Savonius water turbine. *Appl. Energy* **2011**, *88*, 3207–3217. [CrossRef]
35. Tian, W.; Bian, J.; Yang, G.; Ni, X.; Mao, Z. Influence of a passive upstream deflector on the performance of the Savonius wind turbine. *Energy Rep.* **2022**, *8*, 7488–7499. [CrossRef]
36. Chong, W.T.; Muzammil, W.K.; Ong, H.C.; Sopian, K.; Gwani, M.; Fazlizan, A.; Poh, S.C. Performance analysis of the deflector integrated cross axis wind turbine. *Renew. Energy* **2019**, *138*, 675–690. [CrossRef]
37. Kang, C.; Zhao, H.; Zhang, Y.; Ding, K. Effects of upstream deflector on flow characteristics and startup performance of a drag-type hydrokinetic rotor. *Renew. Energy* **2021**, *172*, 290–303. [CrossRef]
38. Lahooti, M.; Kim, D. Multi-body interaction effect on the energy harvesting performance of a flapping hydrofoil. *Renew. Energy* **2019**, *130*, 460–473. [CrossRef]
39. Liu, Z.; Tian, F.B.; Young, J.; Lai, J.C. Flapping foil power generator performance enhanced with a spring-connected tail. *Phys. Fluids* **2017**, *29*, 123601. [CrossRef]
40. Liu, Z.; Bhattacharjee, K.S.; Tian, F.B.; Young, J.; Ray, T.; Lai, J.C. Kinematic optimization of a flapping foil power generator using a multi-fidelity evolutionary algorithm. *Renew. Energy* **2019**, *132*, 543–557. [CrossRef]
41. Xu, L.; Tian, F.B.; Young, J.; Lai, J.C. A novel geometry-adaptive Cartesian grid based immersed boundary–lattice Boltzmann method for fluid–structure interactions at moderate and high Reynolds numbers. *J. Comput. Phys.* **2018**, *375*, 22–56. [CrossRef]
42. Li, W.; Wang, W.Q.; Yan, Y.; Tian, F.B. Effects of pitching motion profile on energy harvesting performance of a semi-active flapping foil using immersed boundary method. *Ocean Eng.* **2018**, *163*, 94–106. [CrossRef]
43. Wang, W.; Yan, Y.; Tian, F.B. Numerical study on hydrodynamics for a non-sinusoidal forced oscillating hydrofoil based on an immersed boundary method. *Ocean Eng.* **2018**, *147*, 606–620. [CrossRef]
44. Filippas, E.S.; Belibassakis, K.A. A nonlinear time-domain BEM for the performance of 3D flapping-wing thrusters in directional waves. *Ocean Eng.* **2022**, *245*, 110157. [CrossRef]
45. Anevlavi, D.E.; Filippas, E.S.; Karperaki, A.E.; Belibassakis, K.A. A non-linear BEM–FEM coupled scheme for the performance of flexible flapping-foil thrusters. *J. Mar. Sci. Eng.* **2020**, *8*, 56. [CrossRef]

46. Gauthier, E.; Kinsey, T.; Dumas, G. Rans versus scale-adaptive turbulence modeling for engineering prediction of oscillating-foils turbines. In Proceedings of the 21th Annual Conference of the CFD Society of Canada, Sherbrooke, QC, Canada, 6–9 May 2013; p. CFDSC2013-186.
47. Badoe, C.E.; Xie, Z.T.; Sandham, N.D. Large Eddy simulation of a heaving wing on the Cusp of transition to turbulence. *Comput. Fluids* **2019**, *184*, 64–77. [CrossRef]
48. Wu, X.; Zhang, X.; Tian, X.; Li, X.; Lu, W. A review on fluid dynamics of flapping foils. *Ocean Eng.* **2020**, *195*, 106712. [CrossRef]
49. Li, G.; Xu, W.; Li, Y.; Wang, F. Univariate analysis of scaling effects on the aerodynamics of vertical axis wind turbines based on high-resolution numerical simulations: The Reynolds number effects. *J. Wind. Eng. Ind. Aerodyn.* **2022**, *223*, 104938. [CrossRef]
50. Samadi, M.; Hassanabad, M.G.; Mozafari, S.B. Performance enhancement of low speed current Savonius tidal turbines through adding semi-cylindrical deflectors. *Ocean Eng.* **2022**, *259*, 111873. [CrossRef]
51. Maldar, N.R.; Yee, N.C.; Oguz, E.; Krishna, S. Performance investigation of a drag-based hydrokinetic turbine considering the effect of deflector, flow velocity, and blade shape. *Ocean Eng.* **2022**, *266*, 112765. [CrossRef]
52. Dabiri, J.O. Theoretical framework to surpass the Betz limit using unsteady fluid mechanics. *Phys. Rev. Fluids* **2020**, *5*, 022501. [CrossRef]
53. Li, Y. On the definition of the power coefficient of tidal current turbines and efficiency of tidal current turbine farms. *Renew. Energy* **2014**, *68*, 868–875. [CrossRef]
54. Mo, W.; He, G.; Wang, J.; Zhang, Z.; Gao, Y.; Zhang, W.; Ghassemi, H. Hydrodynamic analysis of three oscillating hydrofoils with wing-in-ground effect on power extraction performance. *Ocean Eng.* **2022**, *246*, 110642. [CrossRef]
55. *Fluent ANSYS 14.5 Theory Guide*; Ansys Inc.: Canonsburg, PA, USA, 2012.
56. Zheng, X.; Pröbsting, S.; Wang, H.; Li, Y. Characteristics of vortex shedding from a sinusoidally pitching hydrofoil at high Reynolds number. *Phys. Rev. Fluids* **2021**, *6*, 084702. [CrossRef]
57. Simpson, B.J. Experimental Studies of Flapping Foils for Energy Extraction. Ph.D. Thesis, Massachusetts Institute of Technology, Cambridge, MA, USA, 2009.